

The bright blue side of the night sky: Spectroscopic survey of bright and hot (pre-) white dwarfs

Nicole Reindl¹, Ramazan Islami¹, Klaus Werner², S. O. Kepler³, Max Pritzke¹, Harry Dawson¹, Matti Dorsch¹,
Alina Istrate⁴, Ingrid Pelisoli⁵, Stephan Geier¹, Murat Uzundag^{6,7,8}, Judith Provencal^{9,10}, and Stephen
Justham^{11,12,13,14}

¹ Institut für Physik und Astronomie, Universität Potsdam, Haus 28, Karl-Liebknecht-Str. 24/25, D-14476 Potsdam-Golm, Germany

² Institut für Astronomie und Astrophysik, Kepler Center for Astro and Particle Physics, Eberhard Karls Universität, Sand 1, 72076 Tübingen, Germany

³ Instituto de Física, Universidade Federal do Rio Grande do Sul, 91501-970, Porto-Alegre, RS, Brazil

⁴ Department of Astrophysics/IMAPP, Radboud University, P O Box 9010, NL-6500 GL Nijmegen, The Netherlands

⁵ Department of Physics, University of Warwick, Coventry, UK

⁶ Instituto de Física y Astronomía, Universidad de Valparaíso, Gran Bretaña 1111, Playa Ancha, Valparaíso 2360102, Chile

⁷ European Southern Observatory, Alonso de Cordova 3107, Santiago, Chile

⁸ Institute of Astronomy, Faculty of Physics, Astronomy and Informatics, Nicolaus Copernicus University in Toruń, Grudziądzka 5, PL-87-100 Toruń, Poland

⁹ Department of Physics and Astronomy Newark, University of Delaware, DE 19716, USA

¹⁰ Delaware Asteroseismic Research Center, Mt. Cuba Observatory, Greenville, DE 19807, USA

¹¹ Anton Pannekoek Institute for Astronomy and GRAPPA, University of Amsterdam, NL-1090 GE Amsterdam, The Netherlands

¹² School of Astronomy & Space Science, University of the Chinese Academy of Sciences, Beijing 100012, China

¹³ National Astronomical Observatories, Chinese Academy of Sciences, Beijing 100012, China

¹⁴ Max-Planck-Institut für Astrophysik, Karl-Schwarzschild-Straße 1, 85748 Garching, Germany

Received Accepted

ABSTRACT

We report on the spectroscopic confirmation of 68 new bright ($G = 13.5 - 17.2$ mag) and blue (pre-)white dwarfs (WDs). This finding has allowed us to almost double the number of the hottest ($T_{\text{eff}} \geq 60$ kK) known WDs brighter than $G = 16$ mag. We increased the number of known ultra-high excitation (UHE) WDs by 20%, found one unambiguous close binary system consisting of one DA WD with an irradiated low-mass companion, one DAO, and one DOA WD that are likely in their transformation phase of becoming pure DA WDs, one rare, naked O(H) star, two DA and two DAO WDs with T_{eff} possibly in excess of 100 kK, three new DOZ WDs, and three of our targets are central stars of (possible) planetary nebulae.

Using non-local thermodynamic equilibrium models, we derived the atmospheric parameters of these stars and by fitting their spectral energy distribution we derived their radii, luminosities, and gravity masses. In addition, we derived their masses in the Kiel and Hertzsprung–Russell diagram (HRD). We find that Kiel, HRD, and gravity mass agree only in half of the cases. This is not unexpected and we attribute this to the neglect of metal opacities, possibly stratified atmospheres, as well as possible uncertainties of the parallax zero point determination.

Furthermore, we carried out a search for photometric variability in our targets using archival data, finding that 26% of our targets are variable. This includes 15 new variable stars, with only one of them being clearly an irradiation effect system. Strikingly, the majority of the variable stars exhibit non-sinusoidal light-curve shapes, which are unlikely explained in terms of close binary systems. We propose that a significant fraction of all (not just UHE) WDs develop spots when entering the WD cooling phase. We suggest that this could be related to the on-set of weak magnetic fields and possibly diffusion.

Key words. white dwarfs – stars: stars: atmospheres – stars: variables: general – starspots – binaries: close

1. Introduction

Very hot (pre-) white dwarfs (WDs) represent the beginning of the end for the vast majority of all stars. They cover a huge but sparsely populated region in the Hertzsprung–Russell diagram (HRD) and, thus, they are an important link in stellar evolution between the (post-) asymptotic giant branch (AGB) stars, the (post-) red giant branch (RGB) stars, the (post-) extreme horizontal branch (EHB) stars, and the bulk of the cooler WDs. Because the atmospheres of hot pre-WDs (and possibly the

hottest WDs) are not yet affected by gravitational settling of heavier elements (Werner et al. 2020), they are particularly valuable objects in the work to uncover and quantify non-canonical evolutionary pathways, such as the occurrence of (very) late thermal pulses or various double WD merger scenarios (Saio & Jeffery 2000; Werner & Herwig 2006; Justham et al. 2011; Zhang & Jeffery 2012b,a; Reindl et al. 2014b,a; Werner et al. 2022a,b).

Besides their role as key objects in the reconstruction of the various evolutionary histories of intermediate mass stars, very hot pre-WDs also serve as powerful tools to address a multitude of (astro-)physical questions. They are considered the most

Send offprint requests to: Nicole Reindl
e-mail: nreindl1885@gmail.com

reliable and internally consistent flux calibrators (Bohlin et al. 2020) and they serve as laboratories to derive atomic data for highly ionized species of trans-iron elements (e.g., Rauch et al. 2007a, 2015b,a). In addition, newly formed WDs enable the study of the age structure and star formation history of the Galactic halo (Kalirai 2012; Kilic et al. 2019; Fantin et al. 2021), investigations of the properties of weakly interacting particles via the shape of the WD luminosity function (Isern et al. 2008; Miller Bertolami 2014; Miller Bertolami et al. 2014; Isern et al. 2022), and they potentially allow us to directly observe variations in fundamental constants at locations of high gravitational potential (Berengut et al. 2013; Bainbridge et al. 2017; Hu et al. 2020).

The metamorphosis of an AGB or RGB star into a WD is still far from understood. Besides different evolutionary channels, we still do not know whether really every star will go through a planetary nebula (PN) phase, whether PNe are mainly the outcome of a binary phenomenon (Moe & De Marco 2006, 2012; De Marco 2009; Jones 2019; Boffin & Jones 2019), whether the occurrence of PNe is restricted to post-AGB stars only, or whether PNe could also be observed around post-RGB stars (Hall et al. 2013; Hillwig et al. 2017; Jones et al. 2020, 2022).

The transformation of some ($\approx 2/3$) of the He-rich WDs into H-rich at $T_{\text{eff}} \approx 70 - 30$ kK is reasonably well understood (Bédard et al. 2020, 2023). However, it is not yet clear why for $T_{\text{eff}} > 100$ kK, there are $\approx 5\times$ as many H-deficient WDs than H-rich WDs (Fleming et al. 1986; Krzesiński et al. 2009; Werner et al. 2019), while the opposite seems to be the case for pre-WDs (Weidmann et al. 2020) and cooler WDs (Bédard et al. 2020).

The occurrence and evolution of metal abundances in hot WDs is also not yet understood. While Bédard et al. (2022) could aptly reproduce the evolution of the carbon abundances of PG1159 stars into DOZ WDs, their models could not account for the coolest ($\approx 45 - 50$ kK) DOZ stars. Abundances for elements heavier than C are typically derived from ultraviolet (UV) spectra. Some of the hottest WDs still seem to display their original abundance pattern, which is attributed to the presence of a weak residual stellar wind (e.g., Werner et al. 2018b, 2020). For slightly more evolved WDs, diffusion seems to become apparent (e.g., Löbbling et al. 2020; Werner et al. 2018a), meaning light metals (e.g., C, N, and O) have subsolar abundances, while (trans-)iron group elements appear to be enhanced, similar to what is seen in intermediate He-rich hot subdwarfs (e.g. Latour et al. 2018; Dorsch et al. 2019) or (magnetic) chemically peculiar stars (Michaud 1970). It has also been argued that heavy elements are accreted from external sources rather than being intrinsic to the star (Barstow et al. 2014; Schreiber et al. 2019).

Perhaps the strangest phenomenon associated with hot WDs is the sudden appearance of as-yet unidentified absorption lines in the optical spectra of these stars. These absorption lines were tentatively identified as Rydberg lines of ultra-high excited (UHE) metals in ionization stages $v - x$, indicating line formation in a dense environment with temperatures near 10^6 K (Werner et al. 1995). Based on the discovery of photometric and spectroscopic variable UHE WDs, Reindl et al. (2019) suggested that the UHE lines could be created in a wind-fed and shock-heated magnetosphere. Furthermore, UHE WDs were established a new class of variable stars (Reindl et al. 2021). Due to the lack of increasing photometric amplitudes towards longer wavelengths, as well as the non-detection of spectral features of a hypothetical secondary, Reindl et al. (2021) suggested that

spots on the surfaces of these stars and/or geometrical effects of circumstellar material might be responsible.

Interestingly, in recent years there have been increasing indications that also ordinary (non-UHE) hot WDs could be infested with spots. Hermes et al. (2017) reported about a few hot ($T_{\text{eff}} > 30$ kK) magnetic WDs found to be variable in the *K2* mission. Their light curves are either asymmetrical or, as in the case of the 60 kK DAH WD, there are two uneven maxima observed. Furthermore, Werner et al. (2019) found that the extremely hot (105 kK) DA WD PG 0948+534 is photometrically variable with a period of 3.45 d and an asymmetrical light curve shape, which could be explained by spots. Studying the TESS light curves of central stars of PNe, Aller et al. (2020) reported that the light curve of the DO WD PG 1034+001 shows two uneven maxima, which could also be explained with spots.

A major obstacle to making progress with the above-mentioned problems is the small number of known hot (pre-)WDs. In particular bright objects that allow for in-depth investigations, such as detailed metal abundance measurements, search for magnetic fields, or pulsations, are very rare. Thanks to the *Gaia* space mission (Gaia Collaboration et al. 2016, 2021, 2022) and catalogs compiled for hot subdwarfs (i.e., hot pre-WDs) by Geier et al. (2019); Culpan et al. (2022) and catalogs compiled for WDs by Gentile Fusillo et al. (2019, 2021), it has now become possible to search for such objects in a targeted manner.

Motivated to increase especially the number of bright (pre-)WDs on record, we carried out spectroscopic surveys using various telescopes, which are described in Sect. 2. In Sect. 3, we describe the spectral classifications of our targets as well as their positions in the *Gaia* color-magnitude-diagram (CMD). The spectral analysis and the spectral energy distribution (SED) fitting of our stars is explained in Sect. 4 and Sect. 5, respectively. In Sect. 6 we derive the gravity, Kiel, and HRD masses of our stars. In Sect. 7, we investigate archival light curves and search for period signals. Notes on individual objects are provided in Sect. 8. Finally, we provide a summary and a discussion in Sect. 9.

2. Observations

We obtained the spectra of hot (pre-)WD candidates reported by Geier et al. (2019); Culpan et al. (2022); Gentile Fusillo et al. (2019), and Gentile Fusillo et al. (2021) using various observing programs and telescopes, as listed below. In total, we took spectra of 71 individual stars, of which 68 are new discoveries. About two third of the stars have *Gaia* G-band magnitudes between 15 – 16 mag, twelve have $14 < G/\text{mag} < 15$, six have $13.4 < G/\text{mag} < 14$, and eight are fainter than $G = 16$ mag. An overview of all the relevant observations is given in Table A.1.

2.1. Isaac Newton Telescope

We carried out a survey targeting bright and blue WD candidates from the *Gaia* DR2 and eDR3 (ProgID: ING.NL.21A.003, PI: Istrate) at the 2.54 m Isaac Newton Telescope (INT) in 2021 on February 15, 16, 17, and June 10 – 13, 2021. We used the long-slit Intermediate Dispersion Spectrograph (IDS) with the grating R400V which provides a resolution of $R = 1450$. This survey obtained spectra of 44 (pre-) WDs.

In addition, spectra of another ten WDs were taken in December 2019 in course of a survey targeting hot subluminous stars within 500 pc (ProgID: ING.NL.19B.005; PI: Istrate/Justham). This survey also employed the INT using the same instrument

setup as mentioned above. Using the Image Reduction and Analysis Facility (IRAF) bias and flat field corrections were applied to the data. The wavelength calibration was performed with Cu-Ne-Ar calibration lamp spectra. In addition we performed flux calibrations of the instrument response function taking atmospheric extinction into account.

2.2. Southern Astrophysical Research telescope

One spectrum was taken with the Goodman High-Throughput Spectrograph (GHTS, Clemens et al. 2004) with a SYZY 400 grating ($R = 1000$) at the Southern Astrophysical Research (SOAR) 4.1-m telescope on Cerro Pachón. We reduced the spectroscopic data using the instrument pipeline¹ including overscan, trim, slit trim, bias, and flat corrections. We employed a method developed by Pych (2004), included in the pipeline, to identify and remove cosmic rays. After that we carried out the wavelength calibration using the He-Ar-Ne comparison lamp exposure that was taken at the same telescope position as our target. A sixth order Legendre function is used to calibrate the pixel-wavelength correspondence using an atlas of known He-Ar-Ne lines.

2.3. Large Binocular Telescope

We carried out another survey dedicated to the discovery of more UHE WDs as a bad weather filler program (ProgIDs: RDS-2021B-010, RDS-2022A-007, PI: Reindl) at the twin 8.4m Large Binocular Telescope (LBT) using the Multi-Object Double Spectrographs (MODS, Pogge et al. 2010). Our targets were required to have $BP - RP < -0.3$ mag, and absolute *Gaia* magnitude between $6 \text{ mag} < M_G < 9 \text{ mag}$, meaning that they should lie approximately in the color magnitude diagram (CMD) region of known UHE WDs as reported by Reindl et al. (2021). Furthermore, most of our LBT targets are short periodic photometric variables, which we previously found in the Zwicky Transient Facility (ZTF) survey DR5. In total, the spectra of ten WDs were obtained.

MODS provides two-channel grating spectroscopy by using a dichroic that splits the light at $\approx 5650 \text{ \AA}$ into separately optimized red and blue channels. The spectra cover the wavelength region $3330 - 5800 \text{ \AA}$ and $5500 - 10\,000 \text{ \AA}$ with a resolving power of $R \approx 1850$ and 2300 , respectively. We reduced the spectra using the modscddred² PYTHON package (Pogge 2019) for basic 2d CCD reductions, and the modsidl³ pipeline (Croxall & Pogge 2019) to extract 1d spectra and apply wavelength and flux calibrations.

2.4. Very Large Telescope

Twelve further hot (pre-)WD candidates were observed within the Hot Faint Underluminous Sky Survey (HOTFUSS, ProgIDs: 0106.D-0259(A), 0110.D-4098(A); PI: Geier), which was carried out as bad weather filler program with the X-shooter instrument at ESO's Very Large Telescope (VLT). In addition, one hot pre-WD was observed with VLT/X-shooter in course of a program targeting hyper-runaway, intermediate-mass stripped helium stars (ProgID: 0109.D-0235(A); PI: Pritzkeleit). The spectra cover the wavelength range $3000 - 10\,000 \text{ \AA}$ and have a re-

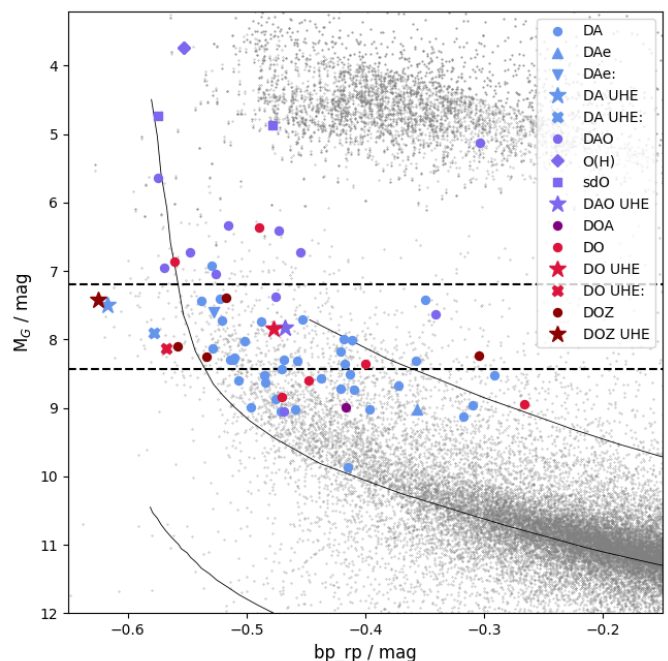


Fig. 1. Locations of our targets in the *Gaia* CMD. Hot subdwarf and WD candidates from Culpan et al. (2022) and Gentile Fusillo et al. (2021), respectively, that have parallaxes better than 10% are shown in gray. The dashed lines indicate the absolute *Gaia* magnitude region in which the UHE phenomenon occurs as uncovered by Reindl et al. (2021). The thin solid lines correspond to Montreal WD cooling tracks for WD masses of 0.2 (top right), 0.6 (middle), and 1.3 M_{\odot} (bottom left).

solving power of $R \approx 10\,000$. We downloaded the extracted, wavelength- and flux-calibrated 1D spectra from the ESO science archive.

3. Spectral Classifications

Ultimately, 80% of our targets turned out to be H-rich, of which we classified 37 as DA; 1 as DAE; 1 as DAE; 1 as DA UHE; 1 as DA UHE; 11 as DAO; 1 as DAO UHE; 1 as an O(H) star; and 2 as sdO stars. The remaining 20% are H-deficient WDs, of which we classified 6 as DO; 2 as DO UHE; 1 as DOA; 4 as DOZ; and 1 as DOZ UHE. We list the spectral classification of each star in Table A.1.

In Fig. 1, we show the locations of our targets in the *Gaia* CMD. Stars that do not show any He are indicated in blue, while hybrid stars showing both H and He are shown in light (if H is the dominant element in the atmosphere) or dark (if He is the dominant element in the atmosphere) purple, stars that only show He in red, and He-rich objects that also show metals in dark red. Also shown in this figure are theoretical cooling sequences for H-rich CO-core WDs with masses of 0.2, 0.6, and 1.3 M_{\odot} of the Montreal WD Group⁴ (Bédard et al. 2020). It can be seen that one sdO and one DAO are located within the hot subdwarf cloud, and the O(H) star as well as another DAO lie in the sparsely populated region between the hot subdwarf cloud and the top of the WD banana. Most of our targets have $M_G < 6$ and lie on the top of the WD banana, or slightly redward of it. The latter is most likely due to interstellar reddening, since the stars in our sample have distances that are approximately between 100 – 2200 pc

¹ https://github.com/soar-telescope/goodman_pipeline

² <https://github.com/rwpogge/modsCCDRed>

³ <https://github.com/rwpogge/modsIDL>

⁴ <https://www.astro.umontreal.ca/~bergeron/CoolingModels/>

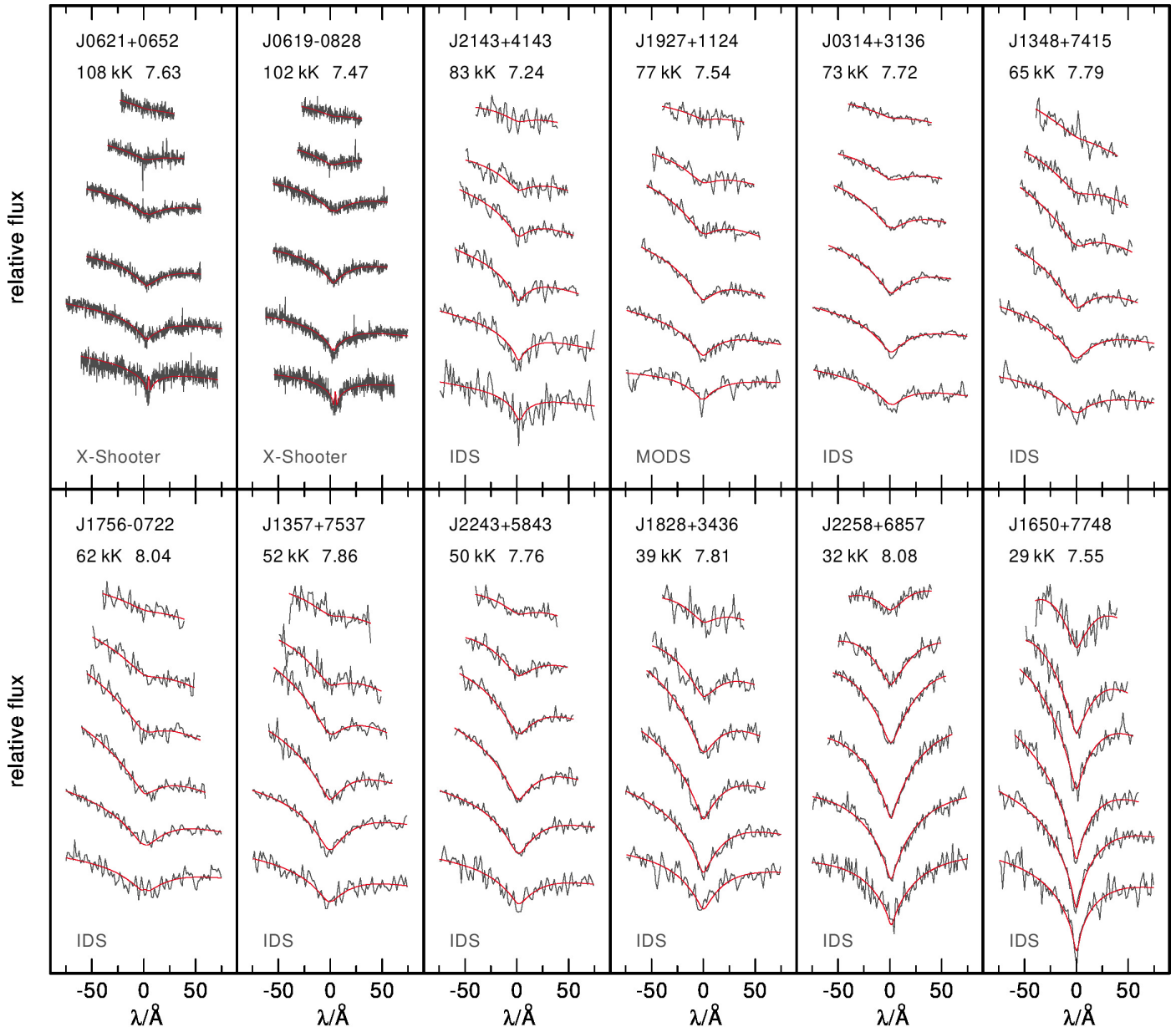


Fig. 2. Fits to the Balmer lines ($H\zeta$ to $H\alpha$, from top to bottom) of some of our DA WDs, overplotted with the best fit TMAP models (red). The names of the stars, the derived effective temperatures and surface gravities as well as the spectrograph used for the observations are indicated.

(Bailer-Jones et al. 2021). It is also worth mentioning that several of our newly discovered UHE WDs (star symbols) and possible UHE WDs (crosses) lie within the absolute *Gaia* magnitude region in which the UHE phenomenon occurs (indicated by the black, dashed lines) as uncovered by Reindl et al. (2021). In addition, we find that several of the DOZ and DAO WDs have M_G below the upper MG limit reported by Reindl et al. (2021) for the UHE WDs. The only exception to this rule is the DAO WD WDJ210110.17–052751.14. However, this object appears to be a former DO WD that is currently transforming into a pure DA WD (see Sect. 9).

4. Spectral Analysis

4.1. Model grids

We computed plane-parallel, non-local thermodynamic equilibrium (NLTE) model atmospheres in radiative and hydrostatic

equilibrium using the Tübingen NLTE Model-Atmosphere Package (TMAP⁵) along with atomic data that were obtained from the Tübingen Model Atom Database (TMAD⁶, Rauch & Deeten 2003; Werner et al. 2003, 2012). To calculate synthetic line profiles, we used Stark line-broadening tables provided by Tremblay & Bergeron (2009) for $H\text{I}$, Barnard et al. (1969) for $\text{He I } \lambda\lambda 4026, 4388, 4471, 4921 \text{ \AA}$, Barnard et al. (1974) for $\text{He I } \lambda 4471 \text{ \AA}$ and Griem (1974) for all other He I lines, and for He II .

The pure H model grid covers $T_{\text{eff}} = 20 - 200 \text{ kK}$ (1 kK steps for $T_{\text{eff}} < 40 \text{ kK}$, 5 kK steps for $T_{\text{eff}} < 100 \text{ kK}$, and 10 kK steps for $T_{\text{eff}} > 100 \text{ kK}$) and $\log g = 6.0 - 9.0$ (in steps of 0.5 dex).

Our pure He model grid spans from $T_{\text{eff}} = 40 - 200 \text{ kK}$ (in steps of 5 kK for $T_{\text{eff}} < 100 \text{ kK}$, 10 kK for $T_{\text{eff}} > 100 \text{ kK}$) and covers surface gravities from $\log g = 6.0 - 9.0$

⁵ <http://astro.uni-tuebingen.de/~TMAP>

⁶ <http://astro.uni-tuebingen.de/~TMAD>

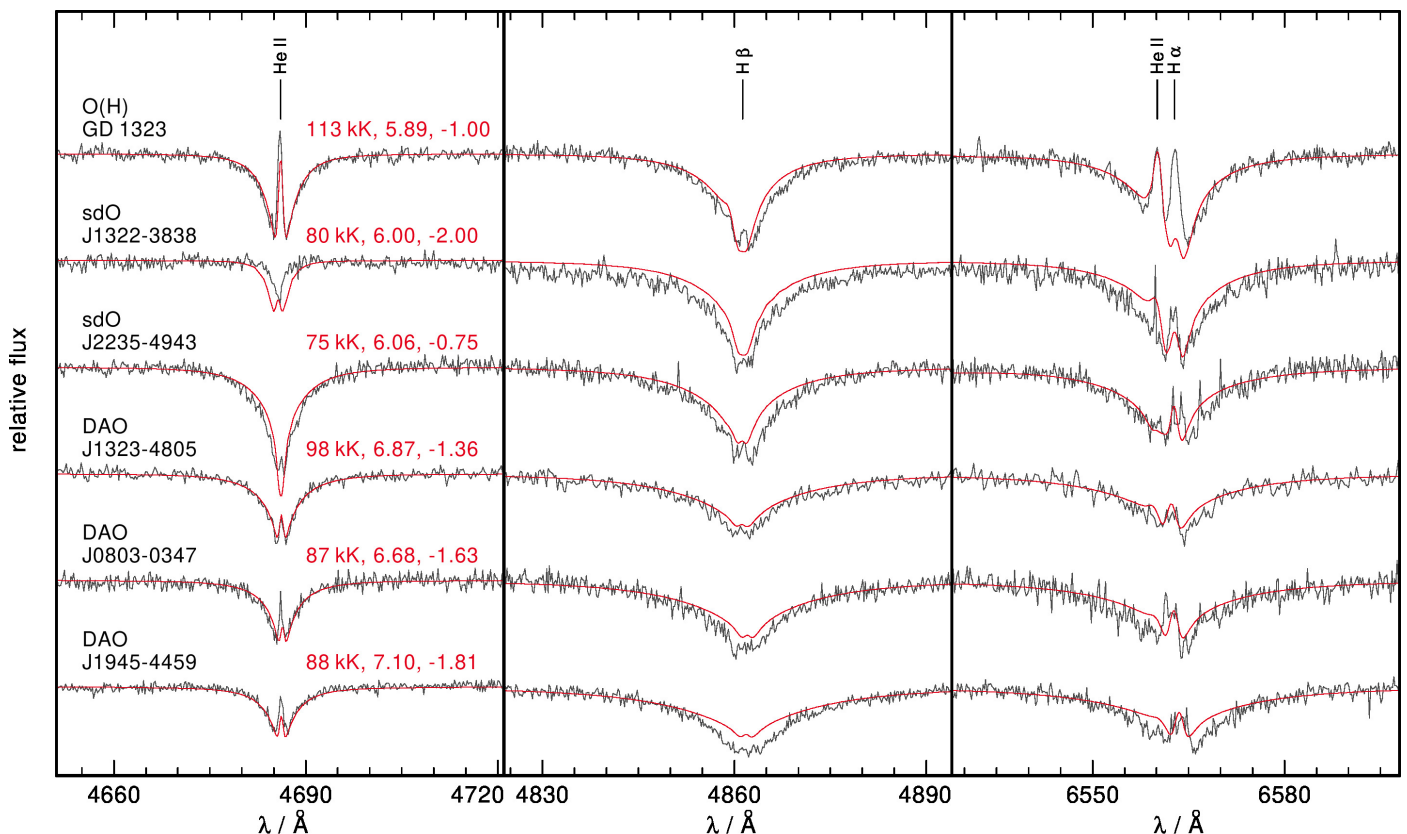


Fig. 3. Fits to He II 4686 Å, H β , and H α observed in the X-Shooter spectra of a selection of our O(H), sdO, and DAO WD stars. Over plotted in red are the best fit TMAP models. The spectral classifications, names of the stars, the derived effective temperatures, surface gravities, and logarithmic He/H ratios (by number) are indicated. The Balmer line problem is more or less evident in each star.

(in steps of 0.5 dex). Models above the Eddington limit (i.e. $T_{\text{eff}} = 190, 200$ kK for $\log g = 6.0$) were not calculated.

For the DOZ WDs, we chose two different model sets, depending on the carbon abundance. For stars with low C/He ratios (≤ 0.03 by number) we computed models composed of helium and carbon. They were described in detail by Werner et al. (2014). For the two DOZs with high carbon abundances (i.e., the PG 1159 stars), we used models composed of He, C, and O, plus H in order to enable an estimate of an upper hydrogen abundance limit. Nitrogen was included and treated as a trace element, meaning that NLTE line formation iterations for N were performed by keeping fixed the atmospheric structure. This model type was introduced by Werner & Rauch (2014).

For DAO WDs we computed a grid which considers opacities from both H and He. It covers the same parameter space and step sizes as the pure He model grid and was calculated for six different He abundances ($\log(\text{He}/\text{H}) = 0, -1, -2, -3, -4, -5$, logarithmic number ratios). Models above the Eddington limit (i.e. $T_{\text{eff}} = 190, 200$ kK for $\log g = 6.0$ and $\log(\text{He}/\text{H}) = 0, -1, -2, -3, -4, -5$, and $T_{\text{eff}} = 180$ kK for $\log g = 6.0$ and $\log(\text{He}/\text{H}) = -2, -3, -4, -5$) were not calculated. For models with $T_{\text{eff}} < 100$ kK, we considered 15, 103, and 20 levels in NLTE for H I He I, and He II, respectively. For models with $T_{\text{eff}} \geq 100$ kK we considered 15, 5, and 32 levels in NLTE for H I He I, and He II, respectively. For stars that turned out to be O(H) or sdO stars, we employed the model grid computed by Reindl et al. (2016).

4.2. Spectral fitting

If more than one spectrum of a star – taken with the same instrument and with a similar signal-to-noise ratio (S/N) – was available, we performed a fit to the co-added spectrum. If the S/N of one spectrum was significantly worse, we only performed a fit to the higher S/N spectrum. Five of our INT targets and the one SOAR target were later re-observed with X-Shooter for the LBT/MODS. For those, we adopted the atmospheric parameters derived in the analysis of the X-Shooter spectra.

To derive the effective temperatures and surface gravities for the DA WDs we fit the Balmer lines in an automated procedure by means of χ^2 minimization using the FITSB2 routine (Napiwotzki 1999) and calculated the statistical 1σ errors. Each fit was then inspected visually to ensure the quality of the analysis. In some cases, for instance, when a certain Balmer line was affected by a cosmic, we excluded this line from the fit. In Fig. 2, we show some examples of these fits and in Table A.2 we summarize the derived effective temperatures and surface gravities for the DA WDs.

For determining T_{eff} , $\log g$, and the He abundances of the DAO WDs, O(H) and sdO stars, we performed global χ^2 spectral fits to consider several absorption lines of H and He. Poor-quality regions of the spectra and interstellar lines have been excluded from the fit. The Balmer line problem is more or less evident in each of these stars as can be seen in Fig. 3, where we show our best fits to He II 4686 Å, H β , and H α in the X-Shooter spectra of some of our DAO WDs, O(H), and sdO stars. The Balmer line problem describes the failure to achieve a consistent fit to all Balmer (and He II) lines simultaneously, meaning that for a particular object different T_{eff} follow from fits to different

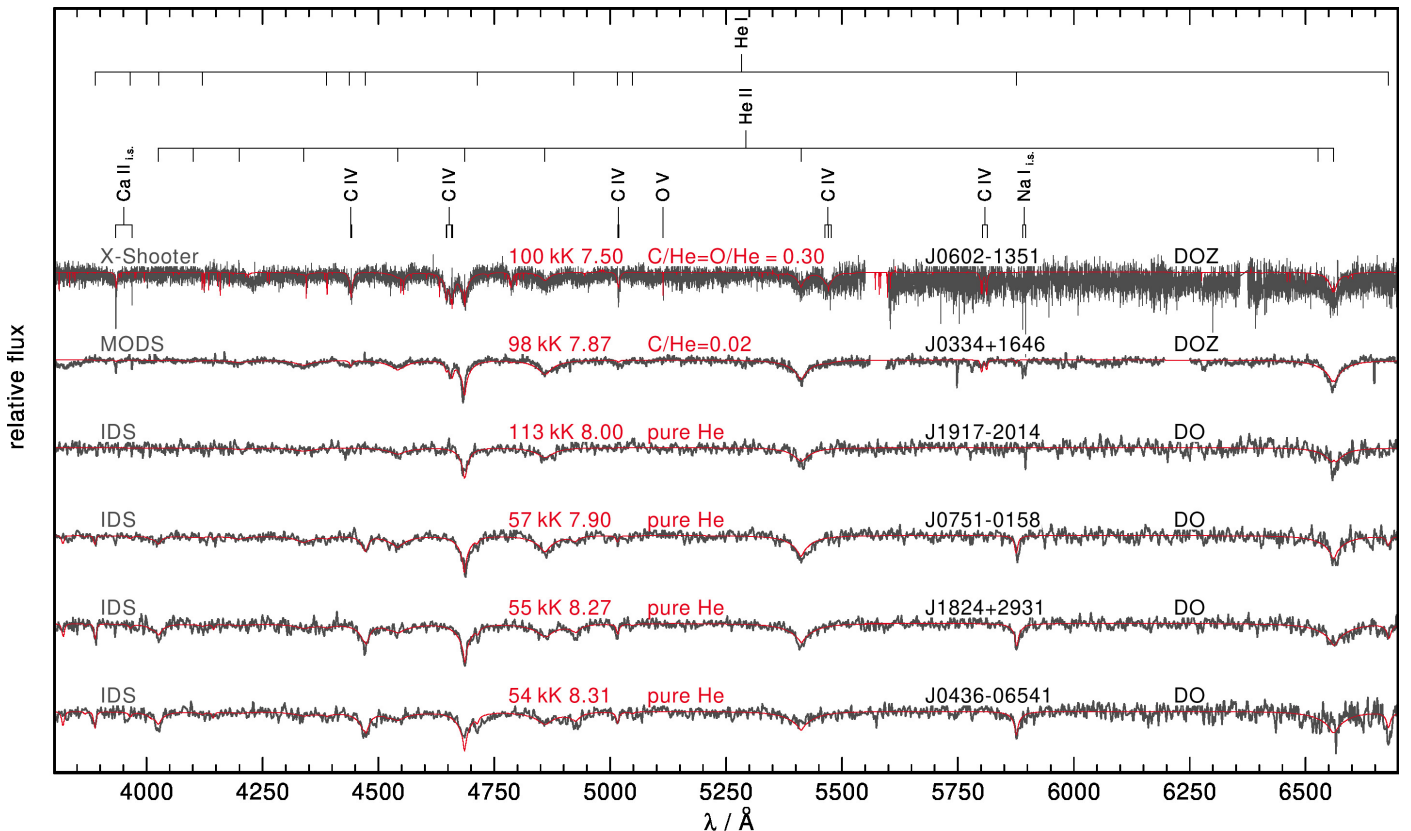


Fig. 4. Spectra of some of the DOZ and DO WDs (gray) overplotted with the best fit TMAP models (red). The positions of photospheric lines are marked. Effective temperatures, surface gravities, and chemical compositions (in number ratios), as determined in this work as well as the spectrograph used for the observation are also indicated.

Balmer line series members. As already mentioned by Bédard et al. (2020), the Balmer line problem can easily hide in low S/N spectra, and for most of our sdO, O(H), and DAO stars, we have higher S/N X-Shooter spectra available. This explains also we find the Balmer line problem more frequent on those stars, compared to the majority of DA WDs, for which we have only INT/IDS spectra. Thanks to the high resolution of X-Shooter, the NLTE line core emissions, whose strength is very sensitive to T_{eff} , are clearly resolved in the spectra of our sdO, O(H), and DAO stars. We provide an overview of the derived atmospheric parameters of the DAO WDs, O(H) and sdO stars in Table A.3.

The same global χ^2 spectral fitting approach as mentioned before has been used to derive the effective temperatures and surface gravities for the DO WDs. In the case of DOZ WDs with low C abundances, we also excluded C IV lines from the fitting. With these parameters, we subsequently computed models including He and C by varying the C abundance to obtain a good by-eye fit to the observed C IV lines in the DOZ stars. We show the fits to a selection of our DO and DOZ WDs in Fig. 4. A summary of the derived effective temperatures, surface gravities, and C abundances is given in Table A.4.

For DOZ WDs with higher C abundances (PG1159 stars), UHE WDs, as well as one of the sdO that shows a particularly strong version of the Balmer line problem, we performed the T_{eff} , $\log g$, and abundance determination by-eye. For a more in-depth description of the fits to each object, we refer to Sect. 8.

5. SED fitting

We performed fits to the SEDs in order to determine the radius, R , and luminosity, L , of each star assuming our previously derived effective temperatures, surface gravities, and He-abundances⁷. In addition, we relied on *Gaia* eDR3 (Gaia Collaboration et al. 2021, 2022) parallaxes, which were corrected for the zeropoint bias using the Python code provided by Lindegren et al. (2021)⁸, as well as photometry from various catalogs and archives. The χ^2 SED fitting routine is described in Heber et al. (2018) and Irrgang et al. (2021). It allows us to derive the angular diameter (defined as $\Theta = 2R/(\varpi)$) of each source by performing a fit of the model spectrum to the observed SED. The fits account for the effect of interstellar reddening by using the reddening law of Fitzpatrick et al. (2019). We kept the atmospheric parameters fixed, and let the angular diameter, Θ , and the color excess, $E(44 - 55)$ ⁹ vary freely. Two exemplary SED fits are shown in Fig. 5. The radius was then calculated from the angular diameter, via $R = \Theta/(2\varpi)$, and the luminosity from the radius and the T_{eff}

⁷ We note that for DOZ WDs we neglected the opacity of C, as thus far, we have only implemented grids containing H and/or He for WDs in the SED fitting program.

⁸ https://gitlab.com/icc-ub/public/gaiadr3_zeropoint

⁹ Fitzpatrick et al. (2019) employs $E(44 - 55)$, which is the monochromatic equivalent of usual $E(B - V)$, using the wavelengths 4400 Å and 5500 Å, respectively. For high effective temperatures such as for the stars in our sample $E(44 - 55)$ is identical to $E(B - V)$.

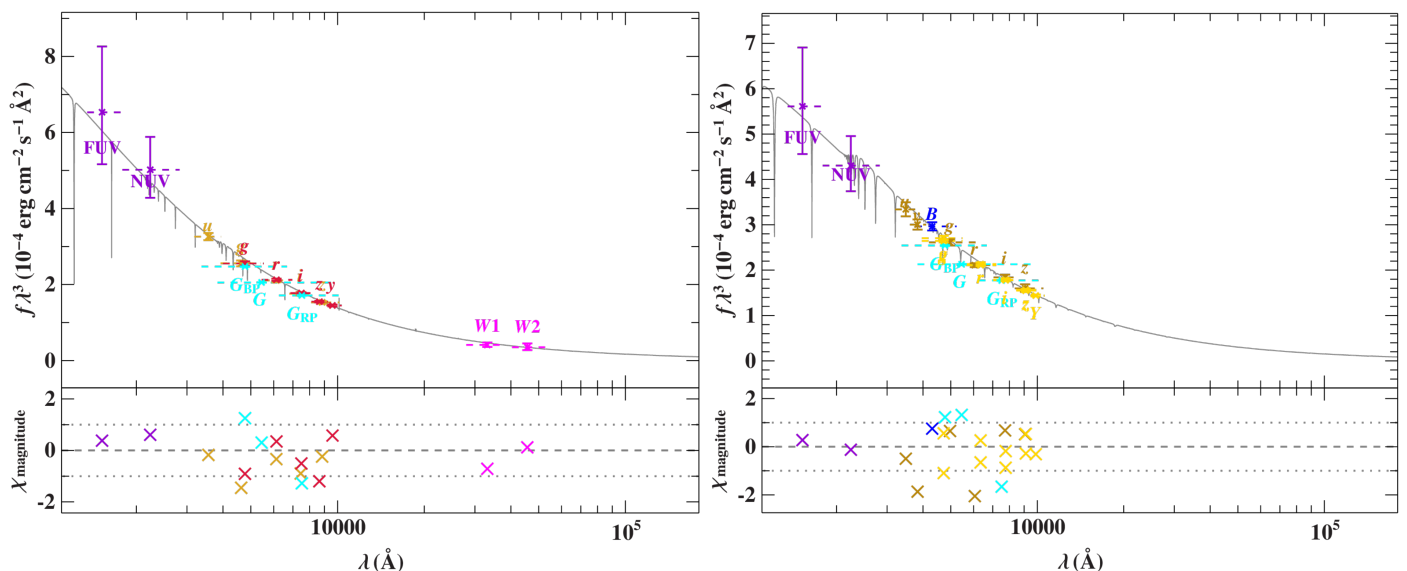


Fig. 5. Exemplary SED fits to the post-RGB candidate DAO central star of PN WDJ120728.43+540129.16 (left) and the DO WDJ211532.62-615849.50 (right). Top panels: Filter-averaged fluxes converted from observed magnitudes are shown in different colors. The respective full width at tenth maximum are shown as dashed horizontal lines. The best-fitting model, degraded to a spectral resolution of 6 \AA is plotted in gray. To reduce the steep SED slope, the flux is multiplied by the wavelength cubed. Bottom panel: Difference between synthetic and observed magnitudes. The following color code is employed for the various photometric systems: GALEX (violet, Bianchi et al. 2017), Pan-STARRS1 (dark red, Chambers et al. 2016), Johnson (blue, Henden et al. 2015), Gaia (cyan, Gaia Collaboration et al. 2021), SDSS (golden, Alam et al. 2015), Skymapper (golden, Wolf et al. 2018), Dark Energy Survey (yellow, Abbott et al. 2018), and WISE (magenta, Schlafly et al. 2019).

from our spectral fitting via $L/L_{\odot} = (R/R_{\odot})^2 (T_{\text{eff}}/T_{\text{eff},\odot})^4$. The derived radii and luminosities¹⁰ are listed in Tables A.2-A.4.

6. Masses

For each star in our sample for which we carried out a formal spectroscopic fit, we determined its mass using three different methods. For one, we derived the Kiel mass, M_{Kiel} , from the Kiel diagram (Fig. 6, left) and HRD mass, M_{HRD} , from the HRD (Fig. 6, right). For this we employed theoretical evolutionary sequences and the griddata function in PYTHON with the rescale option, that rescales the data points of the grid to unit cube before the interpolation is performed. The uncertainties on the Kiel and HRD masses were estimated using a Monte Carlo method. For H-rich objects, we employed evolutionary tracks from Renedo et al. (2010) for CO-core WDs with $Z = 0.01$ and for He-core WDs we used tracks from Hall et al. (2013). For He-rich objects we relied on tracks from Althaus et al. (2009) for CO-core WDs and one track from Camisassa et al. (2019) for a He-rich One-core WD.

Finally, we also calculated the gravity mass via $M_{\text{grav}} = gR^2/G$ from the radius and the surface gravity as determined from the SED fitting and spectral analysis. We list the derived masses in Table A.2-A.4.

7. Light curves

One goal of our observing campaign was to increase the number of UHE WDs. The discovery that the majority ($\approx 75\%$) of these peculiar WDs are photometrically variable (Reindl et al. 2021) provides an important observational constraint that can be used to detect more of these objects.

¹⁰ The numbers given are the median and the highest density interval with probability 0.6827 (see Bailer-Jones et al. 2021, for details on this measure of uncertainty).

Before our observing campaigns and (again) after our spectroscopic analysis, we inspected light curves from the Zwicky Transient Facility (ZTF, Bellm et al. 2019; Masci et al. 2019) survey which provides photometry in the g and r bands, and (with less frequency) in the i -band. In addition, we searched for periodic signals in the 2 min cadence and 20 s cadence light curves obtained with the Transiting Exoplanet Survey Satellite (TESS). We downloaded the TESS target pixel files (TPF) of each object from MAST as FITS format. The FITS files were already processed based on the Pre-Search Data Conditioning Pipeline (Jenkins et al. 2016) from which we extracted the barycentric corrected dynamical Julian days ("BJD - 2457000", a time system that is corrected by leap seconds; see Eastman et al. 2010) and the pre-search Data Conditioning Simple Aperture Photometry flux ("PDCSAP FLUX") for which long-term trends have been removed using the co-trending basis vectors. We used the PDC light curves and converted the fluxes to fractional variations from the mean (i.e., differential intensity).

For the analyses of the light curves, we used the VAR-TOOLS program (Hartman & Bakos 2016) to perform a generalized Lomb-Scargle (LS) search (Zechmeister & Kürster 2009; Press et al. 1992) for periodic sinusoidal signals. We consider objects variable that show a periodic signal with a false alarm probability (FAP) of $\log(\text{FAP}) \leq -4$. In cases where we found more than one significant period, we whitened the light curve by removing the strongest periodic signal (including its harmonics and subharmonics) from the light curve. The periodogram was then recomputed to check whether or not the FAP of the next strongest signal still remains above our variability threshold ($\log(\text{FAP}) \leq -4$). This whitening procedure was repeated until no more significant periodic signals could be found. By fitting a harmonic series (black lines in Fig. 7) to each light curve, we determined the peak-to-peak amplitude of the light curve, which we define as the difference between the maximum and minimum of the fit.

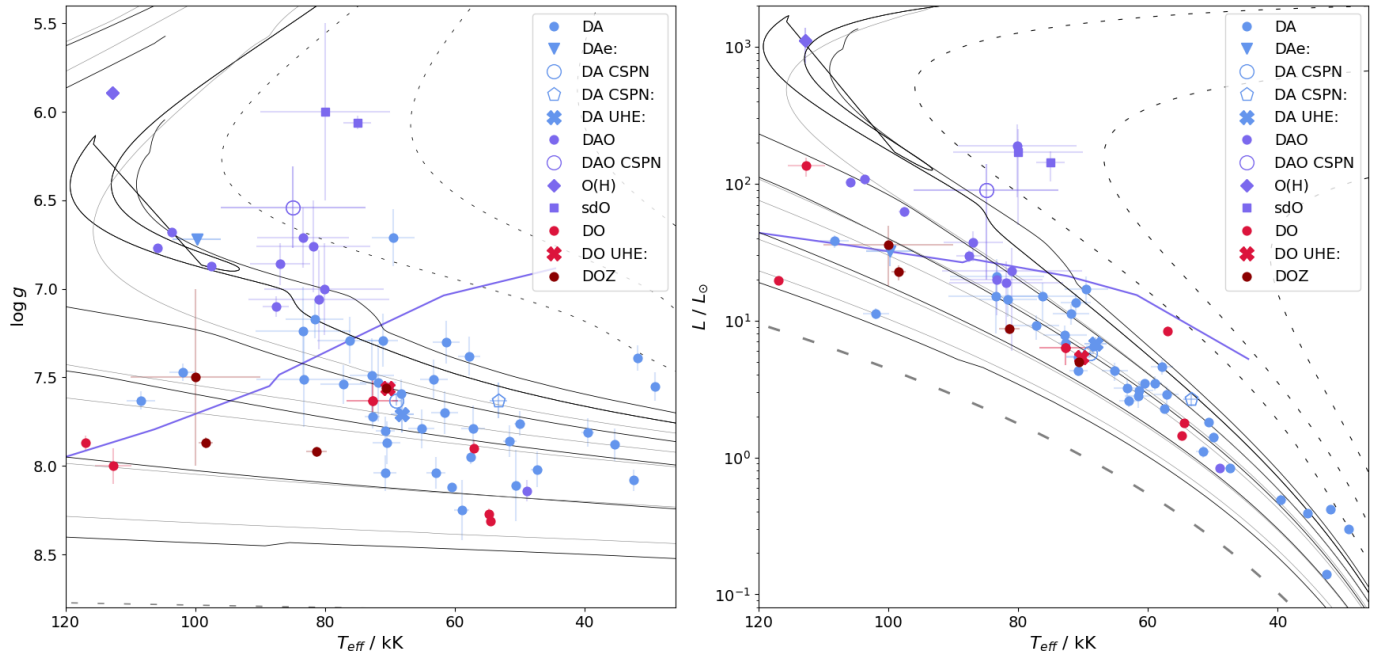


Fig. 6. Locations of our targets in the Kiel diagram (left) and HRD (right). The black dashed and solid lines are stellar evolutionary tracks for He-, CO-core WD, respectively (Renedo et al. 2010; Hall et al. 2013), corresponding to masses of 0.306, 0.378, 0.452, 0.524, 0.570, 0.632, 0.767, and 0.934 M_{\odot} . The gray solid lines are VLTP post-AGB evolutionary tracks from Althaus et al. (2009) for masses of 0.514, 0.565, 0.609, 0.741, and 0.869 M_{\odot} . The gray, thick, dashed line is a 1.10 M_{\odot} H-deficient ONe-Core WD track from Camisassa et al. (2019). The purple solid line indicates where the He abundances should have decreased down to $\log(\text{He}/\text{H}) = -3$ according to predictions of Unglaub & Bues (2000).

Due to the poor spatial resolution (one detector pixel corresponds to 21 arcsec on the sky), TESS photometry suffers from crowding issues. Since our targets are typically faint considering the TESS detection limit, a detected periodic signal of a given target may actually originate from a neighboring object. Therefore we carefully checked for blends with close-by stars using the *tpfplotter* code (Aller et al. 2020) and by checking the crowd-sap parameter, which gives the fraction of the flux in the photometric aperture that comes from our target. In case a star showed variability in the TESS data, but was found to be in a crowded region and no ZTF data was available, we checked the literature for close-by variable stars. Finally, we also employed the open-source Python package *TESS-localize*¹¹ (Higgins & Bell 2023) which allows us to check the probability of a *Gaia* source being the source of variability given TESS pixel data and a set of observed frequencies of variability. We discuss such cases in more detail in Sect. 8.

In Table 1, we summarize the 15 newly discovered photometrically variable stars in our sample, list their spectral type, and the band used for the period search, as well as the amplitude of the light curve variation in each band. We do not list the amplitudes of the TESS light curves as they cannot be considered trustworthy for our faint stars and the large pixel size implies that an accurate background subtraction is very complicated, particularly in crowded fields.

8. Notes on individual objects

8.1. DA WDs

WDJ060020.89–101404.50 The TESS light curve of this 63.2 kK hot DA WD indicates a period of 22.97 h. The star is

¹¹ <https://github.com/Higgins00/TESS-Localize>

located in a crowded field (crowdsap= 0.25), and no ZTF or other archival data are available. However, the Python package *TESS-localize* predicts a likelihood of 1.0 that the WD is indeed the source of observed variability. The shape of the light-curve is asymmetric, with an extended maximum.

WDJ061906.92–082807.15 This is the second hottest DA WD in our sample, we derive $T_{\text{eff}} = 102 \pm 2 \text{ kK}$ and $\log g = 7.47 \pm 0.05$. Fitting $\text{He} \epsilon - \beta$ from low resolution spectra with pure H NLTE models, Vennes (1999) derived a significantly lower $T_{\text{eff}} = 76.3 \pm 0.2 \text{ kK}$ and higher $\log g = 8.05 \pm 0.15$. Since this star only displays a very mild Balmer line problem, the exclusion of $\text{H} \alpha$ from the fit is unlikely the origin of this discrepancy. When we exclude $\text{H} \alpha$ from the fit, we find an slightly higher $T_{\text{eff}} = 103 \text{ kK}$ and that the surface gravity decreases by 0.09 dex. We also note that results from fitting the IDS spectrum ($T_{\text{eff}} = 92 \pm 9 \text{ kK}$ and $\log g = 7.41 \pm 0.18$) agree within the error limits with our results from the analysis of the X-Shooter spectrum. Thus, also the higher resolving power of X-Shooter (that is capable of resolving the NLTE emission cores) cannot explain the much lower T_{eff} derived by Vennes (1999). One might speculate, that the outdated line broadening tables used in the analysis of Vennes (1999) could be responsible for the mismatch in T_{eff} .

WDJ062145.32+065239.25 This is the hottest DA WD in our sample and we find $T_{\text{eff}} = 108 \pm 2 \text{ kK}$ and $\log g = 7.63 \pm 0.05$. Just like WDJ061906.92–082807.15 its T_{eff} is in excess of 100 kK and the star displays only a very mild version of the Balmer line problem, and which only slightly becomes noticeable with the higher resolution and S/N of the X-Shooter spectrum. In the fit to the low-resolution IDS spectrum, we derived a slightly lower temperature ($T_{\text{eff}} = 91 \pm 6 \text{ kK}$), but the surface

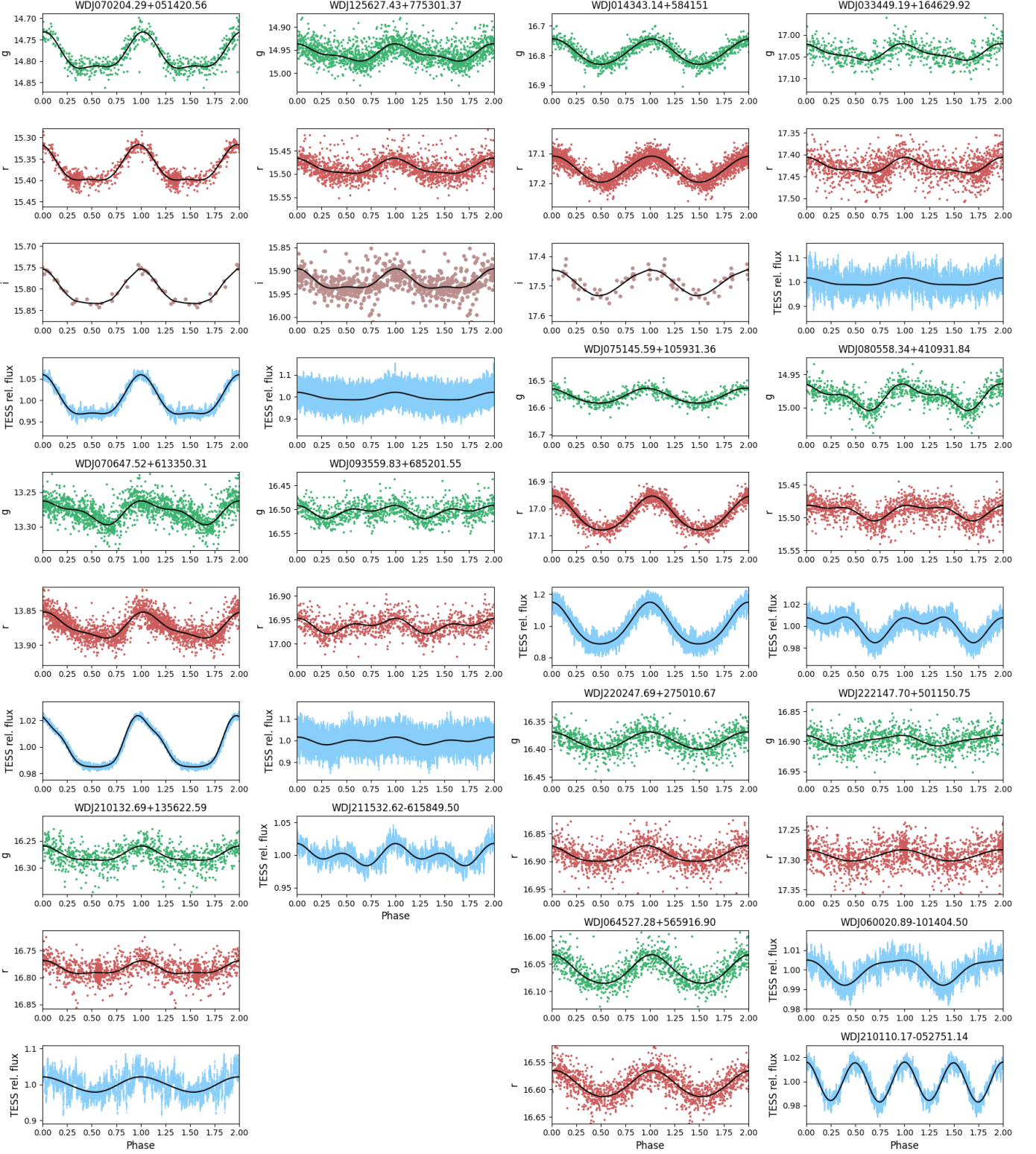


Fig. 7. ZTF and phase-averaged TESS light curves of the photometrically variable stars in our sample. In the first and second column the light curves of (possible) UHE WDs are shown, and in the last two columns the light curves of non-UHE WDs. For each star, the light curves are shown one below the other, and the beginning of a set of light curves for a particular star is marked by the title, which contains the name of the variable star.

gravity ($\log g = 7.47 \pm 0.18$) agrees within the error limits with the fits from the X-Shooter spectrum. We note that the TESS light curve of this star displays photometric variability at 1.91 h. The ZTF light curves of this star contain only 66 and 47 data

points in the g and r band, respectively and no periodic signal can be found. We obtained 3 h of optical high speed photometry using the 0.6 m telescope at Mt. Cuba Astronomical Observatory. The optical data were reduced as outlined in Provencal

Table 1. Names, spectral types, bands of the light curves, periods, and peak-to-peak amplitudes of the light curve variation for the newly discovered photometrically variable stars in our sample.

Name (short)	Spectral Type	Band	P [d]	Amplitude [mag]
J0143+5841	DO	g	0.298152	0.086
		r	0.298152	0.088
		i	0.297917	0.087
J0334+1646	DOZ	g	0.377464	0.038
		r	0.377476	0.036
J0600–1014	DA	TESS	0.957692	
J0645+5659	DAe:	g	1.693849	0.052
		r	1.693875	0.048
J0702+0514	DOZ UHE	g	0.597626	0.083
		r	0.597602	
		i	0.597348	0.083
J0706+6133	DA UHE	TESS	0.598129	
		g	0.373759	0.035
		r	0.373758	0.038
J0751+1059	DAe	TESS	0.373758	
		g	0.276724	0.055
		r	0.276729	0.127
J0805+4109	DA	TESS	0.276728	
		g	0.526120	0.041
		r	0.526115	0.024
J0935+6852	DO UHE	TESS	0.526873	
		g	1.344009	0.028
		r	1.343939	0.032
J1256+7753	DA UHE:	TESS	1.344018	
		g	0.145490	0.037
		r	0.145489	0.032
J2101–0527	DAO	i	0.145491	0.043
		TESS	0.145489	
		TESS	0.537862	
J2101+1356	DAO UHE	g	1.221712	0.026
		r	1.221783	0.024
		TESS	1.218041	
J2115–6158	DO UHE:	TESS	0.620826	
J2202+2750	DA	g	0.815598	0.031
		r	0.815570	0.028
J2221+5011	DA	g	2.272771	0.018
		r	2.272896	0.019

et al. (2012). From this photometry, we concluded that the variability does not originate from the WD but instead comes from a nearby δ Scuti star. In addition, the *TESS-localize* tool also rules out that the WD is the source of the variability.

WDJ080029.42–015039.82 The TESS light curve of this 76.2 kK hot DA indicates a period of 4.92 h and the crowdsap value is 0.53, indicating that at least half of the flux comes from the WD. Yet, Heinze et al. (2018) reports a nearby (1 arcmin away) star, ATO J120.1220–01.8600, which they classify as contact or near-contact eclipsing binary with a period that is exactly twice the period we found. Thus, we conclude that the variability comes from the nearby star – and not the WD.

WDJ080558.34+410931.84 We derived $T_{\text{eff}} = 50.6 \pm 0.2$ kK and $\log g = 8.11 \pm 0.02$ for this DA WD and find that it shows the Balmer line problem. Fitting $H\zeta - \beta$ Gianninas et al.

(2011) derived a slightly higher temperature and lower gravity ($T_{\text{eff}} = 53.2 \pm 1$ kK and $\log g = 7.68 \pm 0.06$). This is likely because they did not have $H\alpha$ available in the fit. When we exclude $H\alpha$ from our fit, we also end up with a slightly higher T_{eff} and lower $\log g$.

This star is photometrically variable with a period of 0.53 d. The ZTF g- and r-band, as well as the TESS light curves, show two uneven minima. Interestingly, the ZTF g band light curve shows two uneven maxima, while the maxima in the ZTF r and TESS band seem similar. We note that the light curves resemble that of the cool (12 kK) and apparently non-magnetic ($B < 70$ kG) WD SDSS J152934.98+292801.9. Kilic et al. (2015) concluded for the latter that it must have a dark spot. In addition, the TESS light curve of the potential young post-merger hot subdwarf, TIC 220490049, displays a similar shape and Vos et al. (2021) concluded, that the variability is explained by a spot on the surface of the star.

WDJ142557.80–034139.92 and **WDJ165053.99+774844.88** are the coolest stars in our sample and both appear to be low-mass – and potentially He-core – WDs based on the derived gravity, HRD, and Kiel masses. We speculate that these stars are the outcome of binary evolution. WDJ142557.80–034139.92 is variable in TESS, however, there is a 7 mag brighter star, Gaia DR3 3642987175954122880, nearby (1 arcmin) and the crowdsap parameter is only 0.05. We also note that *TESS-localize* predicts that the variability comes from Gaia DR3 3642987175954122880 and not the WD. The periodograms of the TESS light curve of WDJ165053.99+774844.88 show several significant peaks at $P > 1$ d. However, *TESS-localize* suggest that these originate from neighbouring stars. This is also in line with the ZTF data, in which we cannot find a significant variability.

WDJ160152.16+380455.24 Pérez-Fernández et al. (2016) reported that it is a sdB candidate that shows an IR excess based on a poor quality 2MASS H band magnitude. We neither confirm the sdB nature of the star nor the IR excess. The 2MASS H and K band magnitudes are merely upper limits and we do not see an excess in the WISE W1 or W2 magnitudes. We find $T_{\text{eff}} = 83 \pm 7$ kK and $\log g = 7.51 \pm 0.27$, which clearly confirms the WD nature of this star.

WDJ182849.94+343649.94 We derived $T_{\text{eff}} = 57.8$ kK and $\log g = 7.38$ for this DA WD. The periodograms of the TESS light curves shows a multitude of significant peaks at $P > 0.6$ d. The crowdsap value is only 0.062 and *TESS-localize* suggests that one of these periods at 2.96 d originates from the WD with a probability of 99.8%. However, we cannot confirm this period based on the ZTF light curves which have 961, 1190, and 82 data points in the g, r, and i bands, respectively. Thus, we classify this star as possibly variable only.

WDJ220247.69+275010.67 Fitting the MODS spectra of this pure DA WD, we derived $T_{\text{eff}} = 58.9 \pm 0.5$ kK and $\log g = 8.25 \pm 0.17$. The star shows the Balmer line problem and the gravity, HRD, and Kiel masses disagree with each other (see Table A.2). Furthermore, we found this star to be periodically variable in the ZTF g- and r-band with a period of 0.82 d. The light curves look approximately sinusoidal, however, the ZTF r-band light curve possibly shows an extended minimum (see

Fig. 7). There is no significant difference in the amplitudes in both bands and there are no hints of a possible companion in the spectrum.

WDJ222147.70+501150.75 This DA WD is the second faintest ($G = 17.01$ mag) star in our sample. A fit to the MODS spectra suggests $T_{\text{eff}} = 57.5 \pm 0.5$ kK and $\log g = 7.95 \pm 0.04$. The Balmer line problem is apparent in this WD, but within the error limits the gravity, HRD, and Kiel masses agree with each other. The ZTF g- and r-band light curves of this DA WD indicate a period of 2.3 d. The amplitudes in both bands are the same and we do not see any hints of emission lines arising from the irradiated side of a hypothetical secondary.

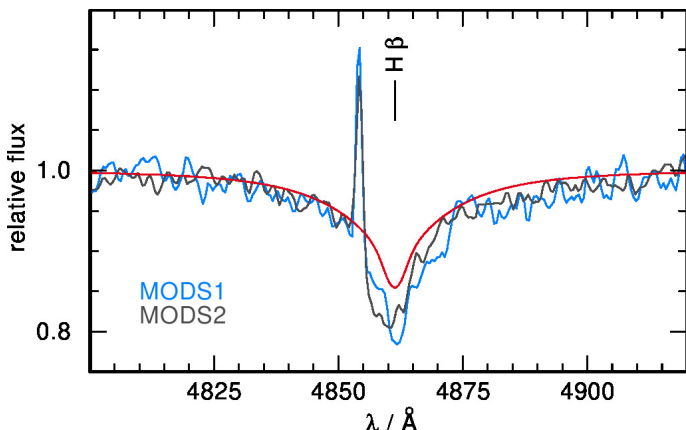


Fig. 8. LBT/MODS1 (blue) and MODS2 (gray) spectra of the DAe: WD WDJ064527.28+565916.90 taken simultaneously and overplotted with the best fit TMAP model (red). The origin of the emission line located on the blue wing of H β remains unclear. No emission lines are visible at the other Balmer line members.

8.2. DAe WDs

WDJ064527.28+565916.90 We classify this star as DAe: WD. Fitting the MODS spectra with pure H TMAP models, we found $T_{\text{eff}} = 99.7 \pm 3.7$ kK and $\log g = 6.72 \pm 0.03$. Moreover, we uncovered a strong Balmer line Problem, which could be related to a cool companion which adds significant flux to the spectrum. The star shows no emission in H α , however, both MODS spectra show a clear emission line located on the blue wing of H β (see Fig. 8). The relative RV shift of this emission line and the H β absorption line from the WD is estimated to be 450 km/s.

The ZTF g- and r-band light curves indicate a photometric variability of 1.69 d and the light curve looks sinusoidal, with no significant difference in the amplitudes in both bands. The star also has TESS 2 min and 20 s cadence light curves, predicting a period of 2.54 h. However, we believe that this signal comes from Gaia DR3 100108833316304512, which is located only 7 arcsec away. This star is reported to be a pulsating variable in the *Gaia* DR3 Part 4 Variability catalog with the same period found by us in the *TESS* data. This is also supported by *TESS*-*localize*.

Assuming the emission line stems from an irradiated companion and the 1.69 d periodicity found in the ZTF lightcurves reflects the orbital period, then the relative RV shift would be unrealistically high. It is also unlikely that the emission line is caused by a cosmic, since it is visible in both (simultaneously taken) MODS spectra. Furthermore, we note that immediately after the spectra of WDJ064527.28+565916.90 were taken, another four

WDs in our sample have been observed within the same night (Table A.1). None those spectra show this emission line blueward of H β , which rules out a data reduction artefact or a sky line.

WDJ075145.59+105931.36 is a DAe WD. The whole Balmer line series as well as He I $\lambda 5876$ Å is seen in emission (see Fig. 9). The relative RV shift of the WD absorption lines and the emission lines is estimated to be 200 km/s. Based on ZTF light curves we find a period of 6.64 h. The amplitude in the ZTF g band is found to be 0.05 mag, much less than in the ZTF r band (0.13 mag), indicating a reflection effect. Since the companion is expected to add significant flux in the optical spectrum, we refrain from a formal fit.

8.3. Central stars of (possible) PN

WDJ120728.43+540129.16 is the DAO type central star of the planetary nebula PN G136.7+61.9. It was first listed as candidate PN by Yuan & Liu (2013), and its true PN nature has been confirmed in 2021 by deep amateur imagery (Le Dû et al. 2022). In Fig. 10, we show a R, G, B, [O III], and H α composite image of the PN as obtained by the amateur astronomer Boris Chausov using a Starlight XPress Trius-SX694 CCD camera mounted on a Celestron Schmidt-Cassegrain telescope. The total integration time of the image is 32.5 h. Assuming a distance of 1173 pc from Bailer-Jones et al. (2021) as well as an expansion velocity of 20 km/s, we find a radius of 1.2 pc and an age of 58 kyrs.

Based on the INT/IDS spectrum, we derived, for the first time, the atmospheric parameters of the CS and find $T_{\text{eff}} = 84.9 \pm 11.2$ kK and $\log g = 6.54 \pm 0.23$. From the SED fit, (see Fig. 5, left) we derived a radius of $0.0450 R_{\odot}$, and a luminosity of $90^{+70}_{-50} L_{\odot}$. The gravity ($0.26^{+0.20}_{-0.12} M_{\odot}$), HRD ($0.49 \pm 0.09 M_{\odot}$), and Kiel ($0.44 \pm 0.07 M_{\odot}$) masses all suggests that this star could be a candidate for post-RGB CSPNe. Adopting the uncertainty on T_{eff} , we find that the $0.452 M_{\odot}$ track from Hall et al. (2013) suggests a post-RGB age of 59–63 kyrs while the $0.532 M_{\odot}$ post-AGB track for $Z = 0.01$ of Miller Bertolami (2016) predicts an post-AGB age of 78–431 kyrs. Since PNe are visible for typically only a few 10 kyrs, this implies that it should actually be more likely to detect a PN around a high-mass post-RGB star, than a low-mass post-AGB star. Unfortunately, we did not detect any significant light curve variations in the TESS or ZTF light curves that could indicate a close companion.

WDJ182440.85–031959.52 This DA WD is the CS of the very faint and large (the diameter is 1900 arcsec, Frew et al. 2016) planetary nebula PNG 026.9+04.4. Using the distance of 195 pc from Bailer-Jones et al. (2021) and assuming an expansion velocity of 20 km/s, a radius of 0.9 pc and a kinematic age of 44 kyrs can be estimated. Fitting the IDS spectrum with pure H models, we derived $T_{\text{eff}} = 68.9 \pm 0.6$ kK and $\log g = 7.63 \pm 0.03$ and by fitting the SED of the star, we found a radius of $0.0168 R_{\odot}$, and a luminosity of $5.74 L_{\odot}$. The HRD ($0.63 \pm 0.05 M_{\odot}$) and Kiel ($0.58 \pm 0.04 M_{\odot}$) masses agree with each other, but the gravity mass ($0.44 \pm 0.04 M_{\odot}$) is significantly lower than the former two. We also note that the post-AGB age in the Kiel diagram and HRD (≈ 300 –400 kyrs) predicted by the Miller Bertolami (2016) tracks is one order of magnitude higher than what is expected from the kinematic age.

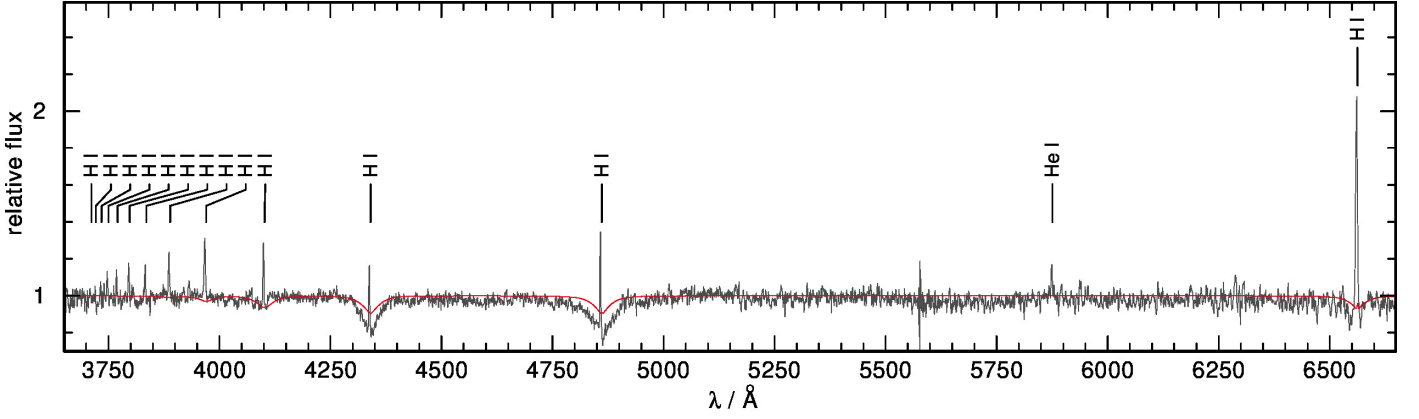


Fig. 9. LBT/MODS spectrum of the newly discovered DAe WD WDJ075145.59+105931.36. The whole Balmer series as well as He I 5876 Å is seen in emission. A pure H TMAP model (red) is overplotted with $T_{\text{eff}} = 100$ kK and $\log g = 8.00$ (note: this is not a formal fit but shown for illustration only).



Fig. 10. Composite R, G, B, [O III], and H α image of the PN G136.7+61.9. The blue star at the center of the PN is the DAO WDJ120728.43+540129.16. The size of the image is 2879x2302 arcsec. Image credit: Boris Chausov.

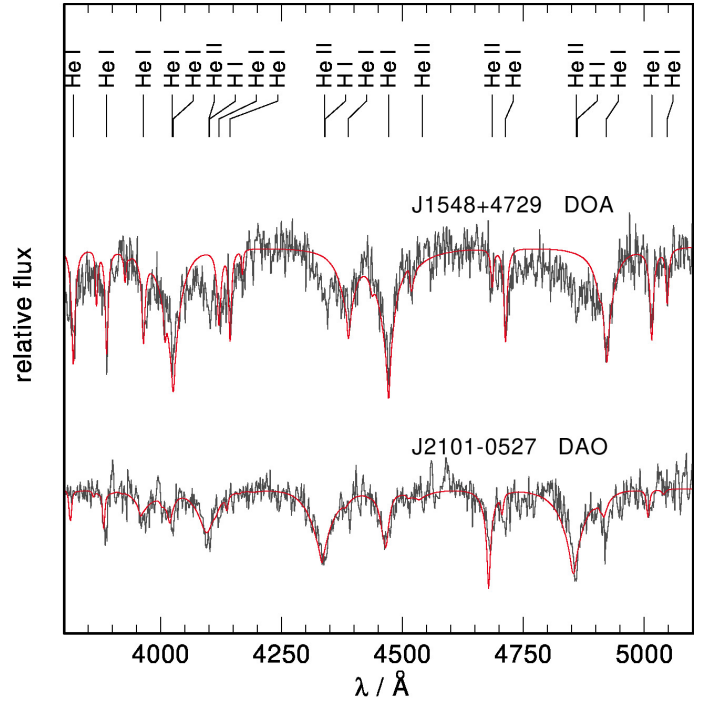


Fig. 11. INT/IDS spectra (gray) of the DOA WD WDJ154843.31+472936.11 (top, overplotted with a pure He model with $T_{\text{eff}} = 40$ kK and $\log g = 7.5$) and the DAO WD WDJ210110.17-052751.14 (bottom, overplotted with a H+He model with $T_{\text{eff}} = 48.9$ kK, $\log g = 8.14$, and $\log(\text{He}/\text{H}) = -0.58$).

WDJ191231.47–033131.86 could be the central star of the possible PN FPJ1912–0331. We derived $T_{\text{eff}} = 53.3 \pm 1.3$ kK and $\log g = 7.63 \pm 0.10$. The gravity ($0.57^{+0.14}_{-0.12} M_{\odot}$), HRD ($0.54 \pm 0.04 M_{\odot}$), and Kiel ($0.55 \pm 0.05 M_{\odot}$) masses agree with each other. From the Miller Bertolami (2016) tracks, we estimate a post-AGB age of 1.2 – 1.5 Myrs, which makes it seem very unlikely that a PNe should still be visible around such a relatively cool WD.

8.4. DAO and DOA WDs

WDJ070322.15–340331.94 and WDJ080950.28–364740.45 are the hottest DAO WDs in our sample and can be considered as twins not only due to their very similar atmospheric parameters, also the Gaia magnitudes and parallaxes are almost the same. For WDJ070322.15–340331.94 we find $T_{\text{eff}} = 105.8$ kK, $\log g = 6.77$, and $\log(\text{He}/\text{H}) = -1.14$ (by number), and for WDJ080950.28–364740.45 we derived $T_{\text{eff}} = 103.6$ kK, $\log g = 6.68$, and $\log(\text{He}/\text{H}) = -1.18$. Their Kiel (0.53 and $0.52 M_{\odot}$, respectively) and HRD (0.58 and $0.56 M_{\odot}$)

masses agree within the error limits, suggesting that they are both post-AGB stars.

WDJ080326.15–034746.11 From the X-Shooter spectrum, we derived $T_{\text{eff}} = 86.9 \pm 4.6$ kK, $\log g = 6.86 \pm 0.12$, and $\log(\text{He}/\text{H}) = -1.63$. From the INT spectrum, we derived a somewhat lower T_{eff} of 69 ± 4.2 kK and higher $\log g = 7.19 \pm 0.19$. Like several of our DAO WDs also this star shows the Balmer line problem (see Fig. 3). The HRD ($0.56 \pm 0.06 M_{\odot}$) and Kiel ($0.50 \pm 0.04 M_{\odot}$) masses agree with each other and suggest that the star is a low-mass post-AGB or post-EHB star. However, the gravity mass ($0.19^{+0.07}_{-0.05} M_{\odot}$) is conspicuously lower than the former two. The TESS light curve

of this DAO WD indicates a period of 5.6 h and the crowdsap value is 0.17. Just as in the case of WDJ080029.42–015039.82, Heinze et al. (2018) reported a nearby (0.8 arcmin) contact or near-contact eclipsing binary system with a period that is exactly twice the period we found. Finally, also *TESS-localize* confirms that the variability does not come from the WD.

WDJ154843.31+472936.11 Comparing a pure He model with $T_{\text{eff}} = 40$ kK and $\log g = 7.5$, we found that the He I lines as well as He II $\lambda 4686$ Å line are well reproduced. However, the observed Balmer lines are stronger than predicted by our model, suggesting that there is some H in the atmosphere of this star (see Fig. 11). Thus, we classify it as DOA WD. Since the star lies at the edge of our grid and most likely has a stratified atmosphere as its T_{eff} is below 45 kK (Bédard et al. 2020), we refrained from carrying out a formal fit.

This star was also observed several time with TESS. The TESS light curve indicates a period of 0.19 d and the crowdsap value is 0.52. However, we cannot confirm this periodicity from ZTF g-, r-, and i-band photometry. The observed period is typical for δ Scuti stars, and also *TESS-localize* confirms that the variability does not come from the WD.

WDJ210110.17–052751.14 This DAO WD shows besides strong Balmer lines also prominent lines of He II and He I, indicating it is one of the rare cooler hybrid WDs. We derived $T_{\text{eff}} = 48.9$ kK, $\log g = 8.14$, and $\log(\text{He}/\text{H}) = -0.58$. As can be seen in Fig. 11, most lines are well reproduced with our model, however, He II $\lambda 4686$ Å is too strong compared to the observation. This is a tell-tale sign that this object is likely to have a stratified atmosphere (Manseau et al. 2016; Bédard et al. 2020). On the other hand, we do not see a problem with He I $\lambda 4471$ Å, which is broader and shallower in stratified models. The analysis should, therefore, be repeated using stratified models as well, in order to test if a better fit can be achieved in this way. Accordingly, we note that these parameters should be treated with caution, because neglecting a stratified atmosphere can lead to large systematic errors. For example, for the hybrid WD SDSS J003343.05+142251.4 Bédard et al. (2020) found $T_{\text{eff}} = 49.2$ kK and $\log g = 8.26$ with homogeneous model atmospheres. When assuming a stratified atmosphere, the derived values dropped down significantly to $T_{\text{eff}} = 40.6$ kK and $\log g = 7.77$.

The 2 min and 20 s cadence TESS light curves of WDJ210110.17–052751.14 indicate a photometric variability with a period of 12.91 h. The crowdsap value is only 0.38. Yet, based on ATLAS c- and o-band light curves, Heinze et al. (2018) reports exactly twice the period that we found in the TESS data, and *TESS-localize* predicts a likelihood of 1.0 that the variability originates from the WD. Interestingly, when folding the TESS light curve to twice the period found in the LS search (1.08 d, i.e., the period reported by Heinze et al. 2018), we found that the depth of the minima differ slightly. In the 2 min and 20 s cadence TESS light curve the difference in the depth of the minima is 0.2% and 0.5%, respectively. Since the star is already very compact ($0.0128 R_{\odot}$), relatively massive (HRD, Kiel, and gravity masses all suggest $M > 0.72 M_{\odot}$), and with a relatively long period, it seems unlikely that the difference in the depth of the minima could be caused by ellipsoidal modulation.

WDJ210824.97+275049.80 We derived for this DAO WD $T_{\text{eff}} = 80.1$ kK, $\log g = 7.00$, and $\log(\text{He}/\text{H}) = -2.01$. The HRD ($0.42 \pm 0.07 M_{\odot}$) and Kiel ($0.50 \pm 0.06 M_{\odot}$) masses agree and make it seem likely that it is a post-EHB star. The gravity mass of this star is again very low ($0.25^{+0.22}_{-0.12} M_{\odot}$), but agrees within the error limits with the Kiel and HRD masses.

8.5. O(H) and sdO stars

GD 1323 We derived $T_{\text{eff}} = 112.7$ kK, $\log g = 5.89$, and $\log(\text{He}/\text{H}) = -1.00$. The Kiel and HRD masses agree and suggest that GD 1323 is a low-mass post-AGB star (Fig. 6), therefore, we considered it as a rare naked (i.e., no PN visible) O(H) star. However, the gravity mass of this star seems again too low. Using the Miller Bertolami (2016) tracks, we estimated a post-AGB age of 27 kyr and 61 kyr from the Kiel diagram and the HRD, respectively. This could be enough time for a former PN to fade into the interstellar medium.

WDJ132259.60-383813.13 and **WDJ223522.88-494350.80** The Kiel and HRD masses of both stars are smaller than $0.50 M_{\odot}$, suggesting that they are either post-RGB or post-EHB stars. We classify these two stars as sdO stars based on their position in the Kiel diagram. When looking into the HRD, however, it could be the case that both stars have recently entered the WD cooling stage and consequently could already be WDs. WDJ132259.60-383813.13 shows a particularly strong version of the BP. Automated fitting attempts showed that the parameters lie at the edge of our DAO grid in terms of $\log g$, and out of the Reindl et al. (2016) grid in terms of He abundances. We estimate $T_{\text{eff}} = 80 \pm 10$ K, $\log g = 6.00 \pm 0.50$, and $X_{\text{He}} = -2.00 \pm 0.50$. Based on the sub-solar He abundance one could speculate, that gravitational settling of He has already started. For WDJ223522.88-494350.80 we find $T_{\text{eff}} = 75.0 \pm 2.2$ kK, $\log g = 6.06 \pm 0.04$, and that the He abundance is slightly enhanced with respect to the solar value. Also, this star shows the Balmer line problem and the observed He II $\lambda 4686$ Å shows a central emission, which is not reproduced by our best-fit model (Fig. 3).

8.6. (Possible) UHE WDs

WDJ070204.29+051420.56 is the second brightest UHE WD known thus far. Based on the IDS spectrum of this star, we estimate $T_{\text{eff}} = 100$ kK, $\log g = 7.50$, and $\text{C}/\text{He} = 0.3$ (number ratio). It is worth noticing that it is the first UHE WD that clearly shows lines of O IV $\lambda 4632$ Å and O V $\lambda 5114$ Å and we estimated $\text{O}/\text{He} = 0.1$ (number ratio). The TESS and ZTF light curves indicate a period of 0.60 d and the amplitudes in ZTF g-, r-, and i-band light curves do not differ significantly. The shapes of the light curves are typical for what is observed for about one third of the UHE WDs, namely an extended minimum with a possibly second maximum (Reindl et al. 2021).

WDJ070647.52+613350.31 is a rare DA-type UHE WD and one of the highlight discoveries of this survey. With $G = 13.49$ mag it is about two orders of magnitude brighter than all the other known UHE WDs. The star displays a strong Balmer line problem. $\text{H}\gamma$, $\text{H}\beta$ and $\text{H}\alpha$ are best reproduced with $T_{\text{eff}} = 40$ kK and $\log g = 7.00$, while the higher order Balmer line series members suggest $T_{\text{eff}} = 110$ kK and $\log g = 7.00$. Light curves obtained by ZTF and TESS reveal a photometric period

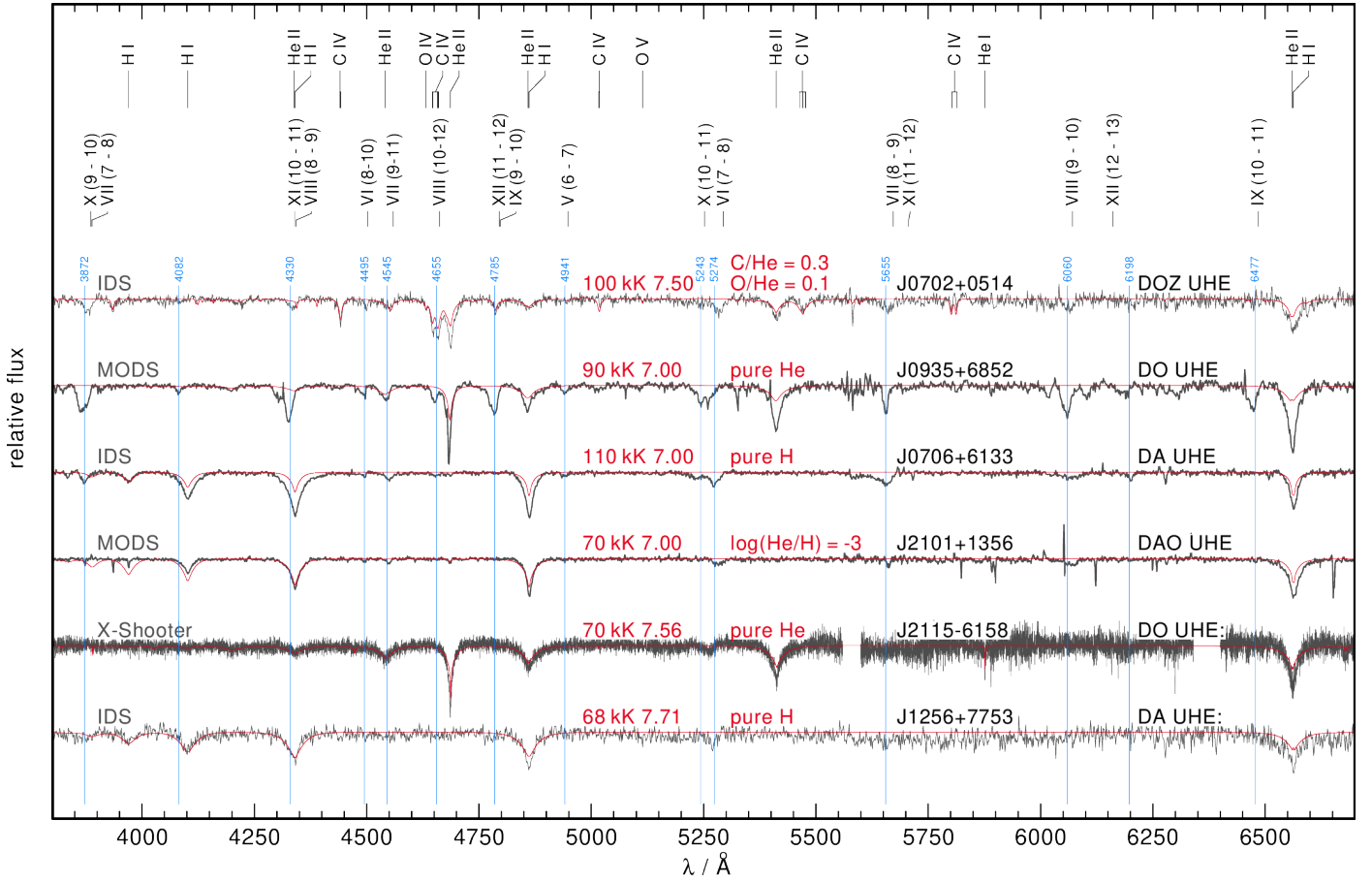


Fig. 12. Spectra of the newly discovered UHE WDs. The positions of photospheric lines (H I, He I, He II, and C IV), α and β transitions between Rydberg states ($n - n'$) of the ionization stages v–x, and approximate line positions of the UHE features (blue) are marked. Over plotted in red are TMAP models and the effective temperatures, surface gravities, and chemical compositions (in number ratios) as determined in this work. The spectrograph used for the observation is indicated in gray.

of 8.97 h, an amplitude of 0.04 mag, and – again – an extended minimum. Interestingly, the ascents and descents to and from the photometric maximum are clearly asymmetrical.

WDJ093559.83+685201.55 We discovered this DO UHE WD at the LBT. The UHE lines are particularly strong in this object and we did not detect any lines of He I nor the C IV $\lambda\lambda$ 5803, 5814 Å doublet. Based on this, we estimated a lower limit on T_{eff} of 90 kK, $\log g = 7.00$, and an upper limit on the C abundance of C/He < 0.002 (by number). The star was observed within ZTF and TESS, and the data from both surveys suggest a period of 1.34 d. The shapes of the light curves resemble that of the DO UHE WD HS 0158+2335. The light curves of this latter object show two maxima, with the first one being at phase 0.0, and the second at approximately phase 0.6, and the minimum is located around phase 0.3 (Reindl et al. 2021).

WDJ125627.43+775301.37 We classified this star as DA UHE: based on the IDS spectrum, which shows possibly a UHE line near 5274 Å. Fitting the spectrum with H models, we found $T_{\text{eff}} = 68.1$ kK and $\log g = 7.71$ and that object shows the Balmer line problem. Based on TESS and ZTF g-, r-, and i-data, we found the star is variable with a period of 3.49 h. The shape of the light curves appears to vary from band to band. In the g-band the light curve looks asymmetrical, while in the i-band it looks more symmetrical with an extended minimum.

WDJ210132.69+135622.59 Based on the MODS spectrum, we classified this star as DAO UHE. Just as WDJ070647.52+613350.31, it displays a strong Balmer line problem. The UHE features are particularly weak in this star (as in the case of, e.g., DAO UHE WD HS 2115+1148 or DO UHE WD HS 0158+2335) and, thus, could have easily been missed in a lower S/N spectrum (LBT/MODS provided us with a S/N of 182). The star is variable in ZTF and TESS with a period of 1.22 d. The ZTF g- and r-band light curve exhibit extended minima.

WDJ211532.62–615849.50 was first observed with SOAR and later with X-Shooter. The star shows the He II line problem and possibly a UHE line near 5274 Å, thus, we classified it a DO UHE: WD. The 2 min and 20 s TESS cadence light curves indicate two significant periods at 7.45 h and at $2 \times 7.45 = 14.90$ h. The crowdsap value is with 0.70 relatively high and *TESS-localize* predicts a likelihood of 1.0 that the WD is indeed the source of observed variability. When folding the light curves to the 7.45 h period, the shapes look approximately sinusoidal, with a possible extended minimum. Yet, when folding the light curves to the 14.90 h period, the light curve is clearly asymmetric with two uneven maxima and minima. Thus, we conclude that the 14.90 h period is likely the rotational period of the star.

8.7. DO(Z) WDs

WDJ014343.14+584151.39 and WDJ191750.16–201409.55 are the hottest DO WDs in our sample with effective temperatures in excess of 110 kK. We were not able to detect lines of C or any other metal in either of them. According to calculations of Unglaub & Bues (2000), who studied the chemical evolution of hot WDs in the presence of diffusion and mass loss, both stars should still display at least half of their original C abundances (meaning the C abundance with which they entered the WD cooling sequence and before it got affected by gravitational settling). Based on this, we can speculate that the H-deficiency in these two DO WDs was not caused by a (very) late thermal pulse, during which large amounts of C are brought to the surface. Instead, these two DO WDs might be the outcome of a double He-WD merger, which predicts only about 1% of atmospheric carbon (by mass). Therefore, they could be the slightly more massive analogs to the DO WDs PG 1034+001 and PG 0038+199 (Zhang et al. 2012; Reindl et al. 2014b; Werner et al. 2017).

We note, however, that the gravity mass of WDJ191750.16–201409.55 is unrealistically high ($3.40^{+1.00}_{-0.80} M_{\odot}$), pointing towards larger systematic uncertainties on the derived parameters. The S/N of the spectrum of WDJ191750.16–201409.55 is only 35, thus it is difficult to judge if the star belongs to the DOs showing the He II line problem, which could be responsible for the unrealistically high gravity mass.

WDJ060244.99–135103.57 The analysis of the INT spectrum of this pulsating PG1159 (GW Vir) star was presented in Uzundag et al. (2021). The authors derived $T_{\text{eff}} = 120 \pm 10$ kK, $\log g = 7.5 \pm 0.5$, $\text{He} = 0.75^{+0.12}_{-0.08}$, and $\text{C} = 0.25^{+0.08}_{-0.12}$ (number fractions). After analyzing the newly obtained X-Shooter spectrum of this star, we confirmed $\log g = 7.5 \pm 0.5$, but with a lower $T_{\text{eff}} = 100 \pm 10$ kK. Thanks to higher resolution of the X-Shooter spectrum, we were able to provide better constraints on the He and C abundances ($\text{He} = 0.72 \pm 0.25$, $\text{C} = 0.21 \pm 0.08$), to derive an upper limit on the H and N abundances ($\text{H} < 0.25$, $\text{N} < 0.0005$), and (for the first time) to derive an O abundance ($\text{O} = 0.07 \pm 0.04$) of this star (all values are number fractions).

WDJ033449.19+164629.92 Based on the MODS spectrum of this DOZ WD, we derived $T_{\text{eff}} = 98.3$ kK, $\log g = 7.87$, and $\text{C}/\text{He} = 0.02$ (by number). The star displays a mild He II line problem (the observed He II $\lambda 6560$ Å line is too broad and deep compared to our best fit model, see Fig. 4), but we find that the Kiel, HRD, and gravity masses agree. The ZTF and TESS light curves indicate a period of 9.06 h. The shapes of the ZTF light curves are clearly asymmetrical and there is no significant difference in the amplitudes in both bands.

WDJ043619.17–065412.61, WDJ075134.71–015807.00, and WDJ182432.46+293115.88 Based on INT/IDS spectra, we found effective temperatures below 60 kK for these three DO WDs. It is worth noting that their gravity masses do not agree with the Kiel and HRD masses. In addition, the HRD and Kiel masses of these stars are inconsistent with each other. We speculate that it could be possible that these stars already have stratified atmospheres.

9. Summary and discussion

We carried out a spectroscopic survey targeting 71 bright ($G = 13.5 - 17.2$ mag) and hot (pre-)WD candidates from the *Gaia* DR2 and eDR3 catalogs of hot subdwarfs (Geier et al. 2019; Culp et al. 2022) and WDs (Gentile Fusillo et al. 2019, 2021). Our main motivation was to increase the number of bright and rare object types (e.g., short-lived pre-WDs in the post-AGB region, UHE WDs, extremely hot, i.e., $T_{\text{eff}} > 60$ kK, WDs, DOZ WDs or photometrically variable WDs) that are suitable for detailed follow-up investigation for instance using high-resolution (UV) spectroscopy, spectropolarimetry, or time-resolved photometry. Out of the 71 stars in our sample, 68 are new discoveries, while for the remaining 3 objects, we obtained spectra with a higher wavelength coverage and/or higher resolution. This allowed us to almost double the number of the hottest ($T_{\text{eff}} > 60$ kK) WDs that are brighter than $G = 16$ mag¹².

Using the *Gaia* eDR3 WD catalog from Gentile Fusillo et al. (2021), we found that 66% of all WD candidates that are brighter than 16 mag and that have $6 < M_G/\text{mag} < 9$ and $\text{bp_rp} < -0.4$ mag have been spectroscopically confirmed and analyzed (either because they have been analyzed in this work or because they are listed with atmospheric parameters in the Montreal White Dwarf Database). In the northern hemisphere ($\text{DEC} > 0$) this percentage is higher (82%) than in the southern hemisphere (48%). Thus, a future survey targeting southern hot WD candidates promises further interesting discoveries. Moreover, we note that additional hot WDs may be hidden at locations of higher reddening or because an unresolved cool companion adds additional flux to the optical or because a cooler companion dominates the optical flux completely.

Using NLTE models we derived the atmospheric parameters of our stars, and by fitting their spectral energy distribution, we derived their radii, luminosities, and gravity masses. In addition, we derived their masses in the Kiel and Hertzsprung–Russell diagram. Furthermore, we have searched for periodic signals in the ZTF and TESS light curves of our stars.

9.1. UHE WDs

Our surveys resulted in the discovery of four, possibly six new UHE WDs (Fig. 12). Previously, only 16 UHE WDs were known (Reindl et al. 2021), thus, we increased the number of known UHE WDs by 20%. We stress that we also discovered the two brightest UHE WDs known and increased the number of H-rich UHE WDs by 67%. With five of the now known twenty UHE WDs being H-rich, we derived the fraction of H-rich UHE WDs as $25.0^{+7}_{-12}\%$. As mentioned earlier, the empirically derived upper M_G limit for UHE WDs seems to coincide with that of DOZ and DAO WDs. Assuming that weak stellar winds keep up C and He in the atmospheres of DOZ and DAO WDs, then it also stands to reason that the UHE phenomenon winds up once the stellar wind has abated. Stellar winds could fade earlier for H-rich objects (Unglaub & Bues 2000), by that the relatively low percentage of H-rich UHE WDs could be understood. Yet, we are still a long way from understanding what could trigger the beginning of the UHE phenomenon.

¹² The Montreal WD database lists 63 WDs with $T_{\text{eff}} > 60$ kK and $\log g < 6.5$ that are brighter than $G = 16$ mag.

9.2. Pure H WDs

Slightly more than a half of the stars in our sample are pure DA WDs and they are found to have effective temperatures ranging from 29 kK to 108 kK. The two coolest DAs in our sample both appear to be low-mass and could be either He-core WDs or post-EHB stars. As a result, they are likely to be the outcome of binary evolution, although we did not find evidence for photometric variability in these two stars. Four of the pure DA WDs were found to be variable, with none of them displaying a hint for a close companion based on the current data. Furthermore, we found one DAe and one DAe:WD, which are both photometrically variable. The latter only shows an emission line located on the blue wind of $H\beta$, and the origin of this line remains unclear. The DAe WD is certainly a close binary system composed of a low-mass companion that is strongly irradiated by the hot DA WD.

9.3. H- and He-rich (pre-)WDs

Our sample includes 16 objects that show both H and He in their spectra. One of them is a rare, naked O(H) star, GD 1323, that is located in the post-AGB region but does not show evidence for a PN. Only 11 of these naked O(H) stars are known (Heber & Kudritzki 1986; Heber & Hunger 1987; Chayer et al. 2015; Bauer & Husfeld 1995; Fontaine et al. 2008; Reindl et al. 2016; Moehler et al. 2019; Jeffery et al. 2023). In the case of GD 1323, we concluded that its post-AGB age is probably long enough for a former PN to fade into the interstellar medium. The Kiel and HRD masses of the two sdO stars in our sample are smaller than $0.50 M_{\odot}$, suggesting that they are either post-RGB or post-EHB stars.

As can be assumed based on Fig. 6, the mean Kiel mass of our DAO WDs ($\langle M_{\text{Kiel}} \rangle = 0.52 M_{\odot}$, $\sigma = 0.01 M_{\odot}$) is lower than the mean Kiel mass of the DA WDs ($\langle M_{\text{Kiel}} \rangle = 0.60 M_{\odot}$, $\sigma = 0.01 M_{\odot}$). This difference is lower but still noticeable in the HRD where we find $\langle M_{\text{HRD}} \rangle = 0.62 M_{\odot}$ ($\sigma = 0.01 M_{\odot}$) for the DA WDs and $\langle M_{\text{HRD}} \rangle = 0.57 M_{\odot}$ ($\sigma = 0.01 M_{\odot}$) for the DAO WDs. It is possible to speculate that this may be related to the striking paucity of H-rich WDs relative to their H-deficient counterparts at the very hot end of the WD cooling sequence (Werner et al. 2019). This is because more massive DAO WDs should have T_{eff} in excess of 100 kK.

Several of our DAO WDs are found to have surface gravities of above 7.10 dex, Kiel masses below $\leq 0.55 M_{\odot}$, and HRD masses $\leq 0.59 M_{\odot}$. The only exception is WDJ210110.17–052751.14 where all three mass determination methods suggest $M \geq 0.72 M_{\odot}$. It is also the only DAO WD that lies within the error limits past the thick purple line in Fig. 6, which indicates where the He abundances should have decreased down to $\log(\text{He}/\text{H}) = -3$ according to predictions of Unglaub & Bues (2000). The star, however, shows the highest He abundance of all DAO WDs in our sample, and – as mentioned earlier – it shows signs of a stratified atmosphere. Thus, we suggest it is a former DO WD that is currently transforming into a DA WD.

Another possible candidate of a transforming WD is the DOA WDJ154843.31+472936.11. It has a T_{eff} around 40 kK and lies at the edge of our grid which is why we did not perform a formal fit. Yet comparing a pure He model to the observed spectrum, we conclude it shows evidence of H and we encourage a fit with stratified model atmospheres.

9.4. Central stars of (possible) PNe

Three of our targets are central stars of (possible) PNe. One of them, WDJ120728.43+540129.16, is a DAO WD, which we consider to be candidate for post-RGB CSPNe. Comparing the predicted post-RGB and post-AGB times of this star with calculations from Hall et al. (2013) and Miller Bertolami (2016), respectively, we found that it actually should be more likely to discover a PN around a post-RGB star than a low-mass post-AGB star. However, we could not reveal any photometric variability (neither in the TESS nor the ZTF light curves) that could hint towards a close companion, which would support the post-RGB nature of this object.

Furthermore, our study revealed the nature of the nucleus of the confirmed PN PNG 026.9+04.4. We found the central star, WDJ182440.85–031959.52, is a pure DA WD and that the post-AGB age ($\approx 300 - 400$ kyrs) predicted by the Miller Bertolami (2016) tracks is one order of magnitude higher than what is expected from the kinematic age.

Finally, our sample also included the pure DA WD WDJ191231.47–033131.86, which could be the central star of the possible PN FPJ1912–0331. Based on the derived atmospheric parameters, we estimated a cooling age around $1.2 - 1.5$ Myrs, which makes it seem very unlikely that a PNe could still be visible.

9.5. He-rich WDs

A fifth of our targets turned out to be H-deficient WDs, of which 13% (and possibly even 19%) show UHE lines. The two hottest ($T_{\text{eff}} > 110$ kK) DO WDs (WDJ014343.14+584151.39 and WDJ191750.16–201409.55), do not show signs of C, and we suggest that they could be the outcome of a double He-WD merger (Zhang & Jeffery 2012b) and, thus, they could be the slightly more massive analogs to the DO WDs PG 1034+001 and PG 0038+199. Five of the H-deficient WDs in our sample are DOZ WDs, with one of them, WDJ060244.99–135103.57, shown to be a previously known pulsating PG1159 (GW Vir) star (Uzundag et al. 2021). Thanks to the higher resolution of the X-Shooter spectrum presented here, we were able to provide better constraints on its T_{eff} ($= 100\,000 \pm 10\,000$ K), to derive its O abundances ($\text{O} = 0.17 \pm 0.10$) and upper limits on the H and N abundances ($\text{H} < 0.05$, $\text{N} < 0.001$). Besides, WDJ060244.99–135103.57, which is known to be variable due to non-radial g -mode pulsations, our work has revealed four newly discovered variable H-deficient WDs, with two of them showing UHE lines.

The mean Kiel mass of our H-deficient WDs ($\langle M_{\text{Kiel}} \rangle = 0.65 M_{\odot}$, $\sigma = 0.01 M_{\odot}$) is slightly higher than the mean Kiel mass of the DA WDs, however, the mean HRD mass of DA and DO WDs ($\langle M_{\text{HRD}} \rangle = 0.63 M_{\odot}$, $\sigma = 0.01 M_{\odot}$) are in agreement. Our mean Kiel mass for DO WDs also agrees with what was previously reported for DO WDs from the SDSS (Bédard et al. 2020).

9.6. Mass determinations

It is important to note that our three mass determinations are not independent from each other. All three methods rely on the results of the spectroscopic analysis. The HRD and Kiel masses additionally depend on stellar evolutionary computations (e.g., core composition and thickness of the H- or He-envelope). In addition, the HRD and gravity masses are both dependent on the

Gaia parallax and the zero point bias.

We find that Kiel and HRD masses agree for 81% of the stars, while the gravity mass agrees with the former two only in half of the cases. This is not unexpected, as the atmospheric parameters of hot (pre-)WDs are known to be prone to systematic effects. To some degree it might be related to the neglect of metal opacities, which can have a large impact on the theoretical Balmer and He II lines and, consequently, on the derived atmospheric parameters – and, thus, the masses. For example, systematic errors on T_{eff} of 10 – 30 kK are not unusual for hot (pre-)WDs (e.g., Rauch et al. 2007b; Gianninas et al. 2010; Reindl et al. 2014b; Werner et al. 2018b,a, 2019). However, it should be noted that even if models including metal opacities are used, the discrepancy in the derived masses may persist (Preval et al. 2019; Herrero et al. 2020; Werner et al. 2022a). In addition the assumption of a homogeneous model atmosphere for a star that actually has a stratified atmosphere can lead to large systematic errors (e.g., Bédard et al. 2020).

We note that the mismatch in the three mass determination methods is not more common in H-rich objects than in He-rich objects or vice-versa. Furthermore, (and quite interestingly) the mismatch is also not more frequent in photometrically variable objects. However, it is striking that the H+He-rich objects in our sample, namely, sdO, O(H), and DAOs, often have a very low gravity mass ($\approx 0.2 M_{\odot}$). In addition, we find that for all DO WDs with $T_{\text{eff}} < 60$ kK the three mass determinations are inconsistent with each other and that their gravity masses are unusually high. We also find that Kiel, HRD, and gravity masses disagree for several stars with T_{eff} in excess of 100 kK. Finally, the discrepancy in the three masses is more common in high S/N spectra, meaning that we found the three masses disagree if the S/N is higher than 50 in 75% of cases.

A quantitative investigation of this problem is well beyond the scope of this paper, however, we would like to briefly discuss possible causes using the example of WDJ080326.15–034746.11. For this star, we found a HRD mass of $0.56 \pm 0.06 M_{\odot}$, a Kiel mass of $(0.50 \pm 0.04 M_{\odot})$, and unrealistically low gravity mass of $0.19^{+0.07}_{-0.05} \pm 0.04 M_{\odot}$. Decreasing T_{eff} by 30 kK would increase the gravity mass only by $+0.10 M_{\odot}$. We note that such a low T_{eff} for this star is unrealistic, since the X-Shooter spectrum clearly revealed the NLTE line emission cores in H α and He II $\lambda 4686 \text{ \AA}$ (see Fig. 3), which would not be expected at $T_{\text{eff}} = 57$ kK. When we assume that the surface gravity has been underestimated by 0.45 dex, then we obtain a gravity mass of $0.54^{+0.19}_{-0.14} M_{\odot}$. Since the surface gravity has barely an impact on the derived radius obtained from the SED fit, also the derived luminosity and, hence, the HRD mass stays essentially the same. On the other hand, with a 0.45 dex higher surface gravity the Kiel mass of the star would increase to $0.56 M_{\odot}$, namely, that it is identical with the HRD mass. However, whether the neglect of metal opacities alone can be responsible for such a significantly higher surface gravity is debatable, for example Gianninas et al. (2010) only obtains a slightly higher values of $\log g$ of ≈ 0.1 dex when models containing CNO are used. In principle, neglecting radiation driven winds can also lead to an underestimation of the surface gravity and, hence, gravity mass. However, given the small mass-loss rates expected in hot WDs, a significant impact on $\log g$ cannot be expected (Sander et al. 2015). Finally, the neglect of metal opacities in our SED fits could also lead to an underestimation of the mass. In models that include metal opacities flux is redistributed from the UV towards longer wavelengths and can lead to an underestimation of the optical (which is our main photometry source for the SED fits) flux from a few to up to 30% (Reindl et al. 2018, 2021). The de-

rived radius relates to the model flux, F_{model} , via $R \propto \sqrt{F_{\text{model}}}$. If we assume that the our models underestimate the optical flux by 10%, then the radius would be underestimated by 5%. In case of WDJ080326.15–034746.11, this would then increase the gravity mass to $0.27 M_{\odot}$, while increasing the luminosity to $41 L_{\odot}$, and decreasing the HRD mass to $0.55 M_{\odot}$.

Besides systematic uncertainties on the atmospheric parameters, which are caused (but not limited to) the neglect of metal opacities, parallax measurements from the *Gaia* mission could also be responsible. In particular, the determination of the parallax bias is non-trivial since it depends at least on the magnitude, colour, and Ecliptic latitude of the source (Lindgren et al. 2021). We note that some of our targets had either pseudo-colours or effective wavenumbers, ν_{eff} , that were outside the parallax correction recipe provided by Lindgren et al. (2021). However, for those targets we do not find that the mismatch of the mass determination methods is more common. We do, however, find there is a slightly higher probability that the derived masses do not agree for lower Ecliptic latitudes. For instance, for $70^{+11}_{-8}\%$ of the stars the gravity, HRD, and Kiel mass do not agree if the Ecliptic latitude is lower than zero, while for Ecliptic latitudes larger than zero, the mismatch of the three masses is only $43^{+7}_{-8}\%$.

Generally, the larger the parallax of a star, the less likely it becomes that the zero point determination is the main source of discrepancy of the derived masses. To test the impact of the zero point bias on the derived masses we take again WDJ080326.15–034746.11 as an example which has a relatively low parallax (1.45 ± 0.05 mas) compared to the rest of our sample. If we assume that the parallax bias has been underestimated by 0.1 mas, then we obtain a 10% larger radius. This, in turn, leads to a higher gravity mass of $0.23 M_{\odot}$, a higher luminosity of $45 L_{\odot}$, and a lower HRD mass of $0.55 M_{\odot}$.

In conclusion, likely a combination of systematic errors on the derived atmospheric parameters that are caused by (but not limited to) the neglect of possibly stratified atmospheres and metal opacities in our spectroscopic and SED fits, as well as the uncertainties of the parallax zero point determination are responsible for the discrepancy of the Kiel, HRD, and gravity masses in some of our stars. Therefore, we would like to appeal to the reader that the parameters of the stars derived in this paper should be treated with caution. They can serve as an first estimate of the atmospheric and stellar parameters, but especially for hot ($T_{\text{eff}} > 50$ kK) H-rich WDs and stars showing the He II problem, it is only with UV spectroscopy that the metal abundances and reliable T_{eff} can be determined, and, thereby, the trustworthy masses.

9.7. Photometric variability

For 62 out of the 71 stars in our sample, there were either TESS and/or ZTF light curves available. Of these 16 (26%) were found to be photometrically variable¹³. One of these objects has been previously reported to be a GW Vir star (Uzundag et al. 2021), but for the remaining 15 we discovered their variability for the first time. Six of the variable stars are (possible) UHE WDs and only one is a clear irradiation effect system consisting of a hot DA WD and an irradiated low-mass companion. Strikingly, the majority (nine out of 15) of the variable stars

¹³ We note that our sample is slightly biased towards variable stars, since our LBT sample (ten stars) contained mainly targets (eight stars) that were known to be variable before the spectroscopic follow-up.

exhibit non-sinusoidal light-curve shapes, with seven showing asymmetrical light curves, and two showing flat and extended minima. This includes all, but is not restricted to (possible) UHE WDs. Such light-curve shapes can unlikely be explained in terms of close binary systems. Instead we propose, that a significant fraction of all stars develop spots at a certain point when entering the WD cooling phase.

Also worth emphasizing is the photometric variability in the DAO WDJ210110.17–052751.14, which is likely currently transforming into a pure DA WD. The light curve looks sinusoidal, but depth of the minima in the TESS light curves of this already very compact and relatively massive star differ slightly, which could be related to two somewhat different sized spots on the surface of the WD.

In three of the stars displaying asymmetrical light curves, we find that the shape (but not the amplitude) of the light curves seems to change from band to band. Such changes are typical for spots and can be explained with different elements which cause their maximum in the light curve at different phases (Krtićka et al. 2020). Furthermore, in the case of metal-enriched spots, the band-to-band amplitude variation is expected typically small. Reindl et al. (2021) predicts band-to-band amplitude variations < 0.04 mag from the g- to z-band for C, O, and iron-group elements. Only in the (near-) UV the difference in the amplitudes can become noticeable. The typical uncertainty of the ZTF light curves is $0.01 - 0.02$ mag, thus, the non-detection of amplitude variations from band to band could still be in line with spots on the surfaces of these stars.

We also note that non-sinusoidal light curves also look very similar to what is observed in magnetic chemically peculiar α^2 Canum Venaticorum variables (ACVs, Hümmerich et al. 2016; Jagelka et al. 2019). Like hot WDs, ACVs possess calm radiative atmospheres and their peculiar abundance patterns are thought to be produced by selective processes, such as radiative levitation and gravitational settling (Richer et al. 2000). Thus, we can speculate that the underlying mechanism of the photometric variability is the same, namely, a magnetic field that interacts with photospheric atoms diffusing under the competitive effects of gravity and radiative levitation (Alecian & Stift 2017). In fact, based on the discovery of spots on extreme horizontal branch (EHB) stars in Galactic globular clusters, Momany et al. (2020) proposed that similar magnetic field induced variability phenomena should take place in all radiative-enveloped hot-stars.

While we did not detect any Zeeman splitting in the spectra of our variable stars, below the detection threshold, field strengths could still be sufficient to enable the production of spots. We highly encourage spectropolarimetric and/or higher resolution follow-up of our variable stars in order to place constraints on the magnetic field strengths.

Yet, the presence of a magnetic field and a radiative atmosphere alone does not seem to be sufficient for the spot production on a hot star. For example, four magnetic ($B \approx 350$ kG) hot subdwarfs were recently discovered, and none of them display photometric variability (Dorsch et al. 2022; Pelisoli et al. 2022). Therefore, at least a third parameter likely determines whether or not a WD develops spots. We speculate whether this could be related to the onset of diffusion.

Acknowledgements. We thank Boris Chausov for providing us with the image of PNG136.7+61.9. We thank Keaton Bell, JJ Hermes, Simon Murphy, and Gerald Handler for useful discussion. NR is supported by the Deutsche Forschungsgemeinschaft (DFG) through grant GE2506/17-1. IP acknowledges funding by the UK's Science and Technology Facilities Council (STFC), grant ST/T000406/1, and from a Warwick Astrophysics prize post-doctoral fellowship, made possible thanks to a generous philanthropic donation. Based on observations with the Isaac Newton Telescopes operated by the Isaac Newton Group at the Observa-

torio del Roque de los Muchachos of the Instituto de Astrofísica de Canarias on the island of La Palma, Spain. This paper uses data taken with the MODS spectrographs built with funding from NSF grant AST-9987045 and the NSF Telescope System Instrumentation Program (TSIP), with additional funds from the Ohio Board of Regents and the Ohio State University Office of Research. IRAF is distributed by the National Optical Astronomy Observatory, which is operated by the Association of Universities for Research in Astronomy (AURA) under a cooperative agreement with the National Science Foundation. This research has made use of the HASH PN database at <http://hashpn.space>. This research made use of TOPCAT, an interactive graphical viewer and editor for tabular data Taylor (Taylor (2005)). This research made use of the SIMBAD database, operated at CDS, Strasbourg, France; the VizieR catalogue access tool, CDS, Strasbourg, France. This research has made use of the services of the ESO Science Archive Facility. This work has made use of data from the European Space Agency (ESA) mission *Gaia* (<https://www.cosmos.esa.int/gaia>), processed by the *Gaia* Data Processing and Analysis Consortium (DPAC, <https://www.cosmos.esa.int/web/gaia/dpac/consortium>). Funding for the DPAC has been provided by national institutions, in particular the institutions participating in the *Gaia* Multilateral Agreement. Based on observations obtained with the Samuel Oschin 48-inch Telescope at the Palomar Observatory as part of the Zwicky Transient Facility project. ZTF is supported by the National Science Foundation under Grant No. AST-1440341 and a collaboration including Caltech, IPAC, the Weizmann Institute for Science, the Oskar Klein Center at Stockholm University, the University of Maryland, the University of Washington, Deutsches Elektronen-Synchrotron and Humboldt University, Los Alamos National Laboratories, the TANGO Consortium of Taiwan, the University of Wisconsin at Milwaukee, and Lawrence Berkeley National Laboratories. Operations are conducted by COO, IPAC, and UW. This paper includes data collected by the TESS mission. Funding for the TESS mission is provided by the NASA Explorer Program. This work made use of *tpfplotter* by J. Lillo-Box (publicly available in www.github.com/jlillo/tpfplotter), which also made use of the python packages *astropy*, *lightkurve*, *matplotlib* and *numpy*.

References

- Abbott, T. M. C., Abdalla, F. B., Allam, S., et al. 2018, *ApJS*, 239, 18
 Alam, S., Albareti, F. D., Allende Prieto, C., et al. 2015, *ApJS*, 219, 12
 Alecian, G. & Stift, M. J. 2017, *MNRAS*, 468, 1023
 Aller, A., Lillo-Box, J., Jones, D., Miranda, L. F., & Barceló Forteza, S. 2020, *A&A*, 635, A128
 Althaus, L. G., Panei, J. A., Miller Bertolami, M. M., et al. 2009, *ApJ*, 704, 1605
 Bailer-Jones, C. A. L., Rybizki, J., Fouesneau, M., Demleitner, M., & Andrae, R. 2021, *AJ*, 161, 147
 Bainbridge, M., Barstow, M., Reindl, N., et al. 2017, *Universe*, 3, 32
 Barnard, A. J., Cooper, J., & Shamey, L. J. 1969, *A&A*, 1, 28
 Barnard, A. J., Cooper, J., & Smith, E. W. 1974, *J. Quant. Spectr. Rad. Transf.*, 14, 1025
 Barstow, M. A., Barstow, J. K., Casewell, S. L., Holberg, J. B., & Hubeny, I. 2014, *MNRAS*, 440, 1607
 Bauer, F. & Husfeld, D. 1995, *A&A*, 300, 481
 Bédard, A., Bergeron, P., & Brassard, P. 2022, *ApJ*, 930, 8
 Bédard, A., Bergeron, P., & Brassard, P. 2023, *arXiv e-prints*, arXiv:2302.05424
 Bédard, A., Bergeron, P., Brassard, P., & Fontaine, G. 2020, *ApJ*, 901, 93
 Bell, E. C., Kulkarni, S. R., Graham, M. J., et al. 2019, *PASP*, 131, 018002
 Berengut, J. C., Flambaum, V. V., Ong, A., et al. 2013, *Physical Review Letters*, 111, 010801
 Bianchi, L., Shiao, B., & Thilker, D. 2017, *ApJS*, 230, 24
 Boffin, H. M. J. & Jones, D. 2019, *The Importance of Binaries in the Formation and Evolution of Planetary Nebulae* (Berlin, New York, Springer-Verlag)
 Bohlin, R. C., Hubeny, I., & Rauch, T. 2020, *AJ*, 160, 21
 Camisassa, M. E., Althaus, L. G., Córscico, A. H., et al. 2019, *A&A*, 625, A87
 Chambers, K. C., Magnier, E. A., Metcalfe, N., et al. 2016, *arXiv e-prints*, arXiv:1612.05560
 Chayer, P., Dixon, W. V., Fullerton, A. W., Ooghe-Tabanou, B., & Reid, I. N. 2015, *MNRAS*, 452, 2292
 Clemens, J. C., Crain, J. A., & Anderson, R. 2004, in *Society of Photo-Optical Instrumentation Engineers (SPIE) Conference Series*, Vol. 5492, *Ground-based Instrumentation for Astronomy*, ed. A. F. M. Moorwood & M. Iye, 331–340
 Croxall, K. V. & Pogge, R. W. 2019, *rwpgge/modsIDL: modsIDL Binocular Release*, Zenodo
 Culpan, R., Geier, S., Reindl, N., et al. 2022, *A&A*, 662, A40
 De Marco, O. 2009, *PASP*, 121, 316
 Dorsch, M., Latour, M., & Heber, U. 2019, *A&A*, 630, A130
 Dorsch, M., Reindl, N., Pelisoli, I., et al. 2022, *A&A*, 658, L9
 Eastman, J., Siverd, R., & Gaudi, B. S. 2010, *PASP*, 122, 935
 Fantin, N. J., Côté, P., McConnachie, A. W., et al. 2021, *ApJ*, 913, 30

- Fitzpatrick, E. L., Massa, D., Gordon, K. D., Bohlin, R., & Clayton, G. C. 2019, *ApJ*, 886, 108
- Fleming, T. A., Liebert, J., & Green, R. F. 1986, *ApJ*, 308, 176
- Fontaine, M., Chayer, P., Oliveira, C. M., Wesemael, F., & Fontaine, G. 2008, *ApJ*, 678, 394
- Frew, D. J., Parker, Q. A., & Bojčić, I. S. 2016, *MNRAS*, 455, 1459
- Gaia Collaboration, Brown, A. G. A., Vallenari, A., et al. 2021, *A&A*, 650, C3
- Gaia Collaboration, Prusti, T., de Bruijne, J. H. J., et al. 2016, *A&A*, 595, A1
- Gaia Collaboration, Vallenari, A., Brown, A. G. A., et al. 2022, *arXiv e-prints*, arXiv:2208.00211
- Geier, S., Raddi, R., Gentile Fusillo, N. P., & Marsh, T. R. 2019, *A&A*, 621, A38
- Gentile Fusillo, N. P., Tremblay, P. E., Cukanovaite, E., et al. 2021, *MNRAS*, 508, 3877
- Gentile Fusillo, N. P., Tremblay, P.-E., Gänsicke, B. T., et al. 2019, *MNRAS*, 482, 4570
- Gianninas, A., Bergeron, P., Dupuis, J., & Ruiz, M. T. 2010, *ApJ*, 720, 581
- Gianninas, A., Bergeron, P., & Ruiz, M. T. 2011, *ApJ*, 743, 138
- Griem, H. R. 1974, *Spectral line broadening by plasmas* (New York, Academic Press, Inc. Pure and Applied Physics. Volume 39, 1974. 421)
- Hall, P. D., Tout, C. A., Izzard, R. G., & Keller, D. 2013, *MNRAS*, 435, 2048
- Hartman, J. D. & Bakos, G. Á. 2016, *Astronomy and Computing*, 17, 1
- Heber, U. & Hunger, K. 1987, *The Messenger*, 47, 36
- Heber, U., Irrgang, A., & Schaffenroth, J. 2018, *Open Astronomy*, 27, 35
- Heber, U. & Kudritzki, R. P. 1986, *A&A*, 169, 244
- Heinze, A. N., Tonry, J. L., Denneau, L., et al. 2018, *AJ*, 156, 241
- Henden, A. A., Levine, S., Terrell, D., & Welch, D. L. 2015, in *American Astronomical Society Meeting Abstracts*, Vol. 225, American Astronomical Society Meeting Abstracts #225, 336.16
- Hermes, J. J., Gänsicke, B. T., Kawaler, S. D., et al. 2017, *ApJS*, 232, 23
- Herrero, A., Parthasarathy, M., Simón-Díaz, S., et al. 2020, *MNRAS*, 494, 2117
- Higgins, M. E. & Bell, K. J. 2023, *AJ*, 165, 141
- Hillwig, T. C., Frew, D. J., Reindl, N., et al. 2017, *AJ*, 153, 24
- Hu, J., Webb, J. K., Ayres, T. R., et al. 2020, *arXiv e-prints*, arXiv:2007.10905
- Hümmerich, S., Paunzen, E., & Bernhard, K. 2016, *AJ*, 152, 104
- Irrgang, A., Geier, S., Heber, U., et al. 2021, *A&A*, 650, A102
- Isern, J., García-Berro, E., Torres, S., & Catalán, S. 2008, *ApJ*, 682, L109
- Isern, J., Torres, S., & Rebassa-Mansergas, A. 2022, *Frontiers in Astronomy and Space Sciences*, 9, 6
- Jagelka, M., Mikulášek, Z., Hümmerich, S., & Paunzen, E. 2019, *A&A*, 622, A199
- Jeffery, C. S., Werner, K., Kilkenny, D., et al. 2023, *MNRAS*, 519, 2321
- Jenkins, J. M., Twicken, J. D., McCauliff, S., et al. 2016, in *Society of Photo-Optical Instrumentation Engineers (SPIE) Conference Series*, Vol. 9913, Software and Cyberinfrastructure for Astronomy IV, ed. G. Chiozzi & J. C. Guzman, 99133E
- Jones, D. 2019, in *Highlights on Spanish Astrophysics X*, ed. B. Montesinos, A. Asensio Ramos, F. Buitrago, R. Schödel, E. Villaver, S. Pérez-Hoyos, & I. Ordóñez-Etxeberria, 340–345
- Jones, D., Boffin, H. M. J., Hibbert, J., et al. 2020, *A&A*, 642, A108
- Jones, D., Munday, J., Corradi, R. L. M., et al. 2022, *MNRAS*, 510, 3102
- Justham, S., Podsiadlowski, P., & Han, Z. 2011, *MNRAS*, 410, 984
- Kalirai, J. S. 2012, *Nature*, 486, 90
- Kilic, M., Bergeron, P., Dame, K., et al. 2019, *MNRAS*, 482, 965
- Kilic, M., Gianninas, A., Bell, K. J., et al. 2015, *ApJ*, 814, L31
- Krtićka, J., Kawka, A., Mikulášek, Z., et al. 2020, *A&A*, 639, A8
- Krzesiński, J., Kleinman, S. J., Nitta, A., et al. 2009, *A&A*, 508, 339
- Latour, M., Chayer, P., Green, E. M., Irrgang, A., & Fontaine, G. 2018, *A&A*, 609, A89
- Le Dú, P., Mulato, L., Parker, Q. A., et al. 2022, *A&A*, 666, A152
- Lindgren, L., Bastian, U., Biermann, M., et al. 2021, *A&A*, 649, A4
- Löbbling, L., Maney, M. A., Rauch, T., et al. 2020, *MNRAS*, 492, 528
- Manseau, P. M., Bergeron, P., & Green, E. M. 2016, *ApJ*, 833, 127
- Masci, F. J., Laher, R. R., Rusholme, B., et al. 2019, *PASP*, 131, 018003
- Michaud, G. 1970, *ApJ*, 160, 641
- Miller Bertolami, M. M. 2014, *A&A*, 562, A123
- Miller Bertolami, M. M. 2016, *A&A*, 588, A25
- Miller Bertolami, M. M., Melendez, B. E., Althaus, L. G., & Isern, J. 2014, *ArXiv e-prints* 1406.7712 [arXiv:1406.7712]
- Moe, M. & De Marco, O. 2006, *ApJ*, 650, 916
- Moe, M. & De Marco, O. 2012, *IAU Symposium*, 283, 111
- Moehler, S., Landsman, W. B., Lanz, T., & Miller Bertolami, M. M. 2019, *A&A*, 627, A34
- Momany, Y., Zaggia, S., Montalto, M., et al. 2020, *Nature Astronomy*, 4, 1092
- Napiwotzki, R. 1999, *A&A*, 350, 101
- Pelisolì, I., Dorsch, M., Heber, U., et al. 2022, *MNRAS*, 515, 2496
- Pérez-Fernández, E., Ulla, A., Solano, E., Oreiro, R., & Rodrigo, C. 2016, *MNRAS*, 457, 3396
- Pogge, R. 2019, *rwpgge/modsCCDRed: v2.0.1*, Zenodo
- Pogge, R. W., Atwood, B., Brewer, D. F., et al. 2010, in *Society of Photo-Optical Instrumentation Engineers (SPIE) Conference Series*, Vol. 7735, Ground-based and Airborne Instrumentation for Astronomy III, ed. I. S. McLean, S. K. Ramsay, & H. Takami, 77350A
- Press, W. H., Teukolsky, S. A., Vetterling, W. T., & Flannery, B. P. 1992, *Numerical recipes in C. The art of scientific computing* (New York: Cambridge University Press)
- Preval, S. P., Barstow, M. A., Bainbridge, M., et al. 2019, *MNRAS*, 487, 3470
- Provencal, J. L., Montgomery, M. H., Kanaan, A., et al. 2012, *ApJ*, 751, 91
- Pych, W. 2004, *PASP*, 116, 148
- Rauch, T. & Deetjen, J. L. 2003, in *Astronomical Society of the Pacific Conference Series*, Vol. 288, Stellar Atmosphere Modeling, ed. I. Hubeny, D. Mihalas, & K. Werner, 103
- Rauch, T., Hoyer, D., Quinet, P., Gallardo, M., & Raineri, M. 2015a, *A&A*, 577, A88
- Rauch, T., Werner, K., Quinet, P., & Kruk, J. W. 2015b, *A&A*, 577, A6
- Rauch, T., Ziegler, M., Werner, K., et al. 2007a, *A&A*, 470, 317
- Rauch, T., Ziegler, M., Werner, K., et al. 2007b, *A&A*, 470, 317
- Reindl, N., Bainbridge, M., Przybilla, N., et al. 2019, *MNRAS*, 482, L93
- Reindl, N., Geier, S., Kupfer, T., et al. 2016, *A&A*, 587, A101
- Reindl, N., Geier, S., & Østensen, R. H. 2018, *MNRAS*, 480, 1211
- Reindl, N., Rauch, T., Werner, K., et al. 2014a, *A&A*, 572, A117
- Reindl, N., Rauch, T., Werner, K., Kruk, J. W., & Todt, H. 2014b, *A&A*, 566, A116
- Reindl, N., Schaffenroth, V., Filiz, S., et al. 2021, *A&A*, 647, A184
- Renedo, I., Althaus, L. G., Miller Bertolami, M. M., et al. 2010, *ApJ*, 717, 183
- Richer, J., Michaud, G., & Turcotte, S. 2000, *ApJ*, 529, 338
- Saio, H. & Jeffery, C. S. 2000, *MNRAS*, 313, 671
- Sander, A., Shenar, T., Hainich, R., et al. 2015, *A&A*, 577, A13
- Schlaflly, E. F., Meisner, A. M., & Green, G. M. 2019, *ApJS*, 240, 30
- Schreiber, M. R., Gänsicke, B. T., Toloza, O., Hernandez, M.-S., & Lagos, F. 2019, *ApJ*, 887, L4
- Taylor, M. B. 2005, in *Astronomical Society of the Pacific Conference Series*, Vol. 347, Astronomical Data Analysis Software and Systems XIV, ed. P. Shopbell, M. Britton, & R. Ebert, 29
- Tremblay, P.-E. & Bergeron, P. 2009, *ApJ*, 696, 1755
- Unglaub, K. & Bues, I. 2000, *A&A*, 359, 1042
- Uzundag, M., Côrsico, A. H., Kepler, S. O., et al. 2021, *A&A*, 655, A27
- Vennes, S. 1999, *ApJ*, 525, 995
- Vos, J., Pelisolì, I., Budaj, J., et al. 2021, *A&A*, 655, A43
- Weidmann, W. A., Mari, M. B., Schmidt, E. O., et al. 2020, *A&A*, 640, A10
- Werner, K., Dreizler, J. L., Dreizler, S., et al. 2003, in *Astronomical Society of the Pacific Conference Series*, Vol. 288, Stellar Atmosphere Modeling, ed. I. Hubeny, D. Mihalas, & K. Werner, 31
- Werner, K., Dreizler, S., Heber, U., et al. 1995, *A&A*, 293, L75
- Werner, K., Dreizler, S., & Rauch, T. 2012, *TMAP: Tübingen NLTE Model-Atmosphere Package*, Astrophysics Source Code Library
- Werner, K. & Herwig, F. 2006, *PASP*, 118, 183
- Werner, K. & Rauch, T. 2014, *A&A*, 569, A99
- Werner, K., Rauch, T., & Kepler, S. O. 2014, *A&A*, 564, A53
- Werner, K., Rauch, T., & Kruk, J. W. 2017, *A&A*, 601, A8
- Werner, K., Rauch, T., & Kruk, J. W. 2018a, *A&A*, 609, A107
- Werner, K., Rauch, T., & Kruk, J. W. 2018b, *A&A*, 616, A73
- Werner, K., Rauch, T., & Reindl, N. 2019, *MNRAS*, 483, 5291
- Werner, K., Reindl, N., Dorsch, M., et al. 2022a, *A&A*, 658, A66
- Werner, K., Reindl, N., Geier, S., & Pritzkeleit, M. 2022b, *MNRAS*, 511, L66
- Werner, K., Reindl, N., Löbbling, L., et al. 2020, *A&A*, 642, A228
- Wolf, C., Onken, C. A., Luvaul, L. C., et al. 2018, *PASA*, 35, e010
- Yuan, H. B. & Liu, X. W. 2013, *MNRAS*, 436, 718
- Zechmeister, M. & Kürster, M. 2009, *A&A*, 496, 577
- Zhang, X. & Jeffery, C. S. 2012a, *MNRAS*, 426, L81
- Zhang, X. & Jeffery, C. S. 2012b, *MNRAS*, 419, 452
- Zhang, Y., Fang, X., Chau, W., et al. 2012, *ApJ*, 754, 28

Appendix A: Tables

Table A.1. Overview of the observations. Name, J2000 coordinates of our targets given along with what telescopes and instruments they have been observed. The MJD at the start of the observation, exposure times and the S/N as measured between 5100 – 5300 Å of the observations are listed as well.

Name	Type	Ra [deg]	Dec [deg]	Telescope/ Instrument	MJD-OBS	T_{exp} [s]	S/N
WDJ014343.14+584151.39	DO V*	25.92974	58.69761	LBT/MODS	59526.31541	900	127
WDJ020351.33–063906.46	DA	30.96387	–6.65179	LBT/MODS	59528.31042	1184	272
WDJ020351.33–063906.46	DA	30.96402	–6.65179	INT/IDS(R400V)	58827.91127	1800	36
WDJ023722.53+583405.41	DA	39.34390	58.56817	INT/IDS(R400V)	59260.91354	1800	51
WDJ031437.37+313641.91	DA	48.65573	31.61164	INT/IDS(R400V)	59260.94453	900	89
WDJ033449.19+164629.92	DOZ V*	53.70498	16.77498	LBT/MODS	59528.33045	900	125
WDJ043619.17–065412.61	DO	69.07988	–6.9035	INT/IDS(R400V)	59262.91673	1800	39
WDJ051351.78–225919.24	DA	78.46576	–22.9887	INT/IDS(R400V)	59261.88301	1800	57
WDJ051949.17–044300.03	DO	79.95486	–4.71667	INT/IDS(R400V)	58825.99324	1800	22
WDJ053810.41–103644.81	DA	84.54339	–10.6124	INT/IDS(R400V)	59261.96735	1800	59
WDJ060020.89–101404.50	DA V*	90.08705	–10.2346	INT/IDS(R400V)	59262.98942	1800	45
WDJ060244.99–135103.57	DOZ V*	90.68749	–13.85096	VLT/X-Shooter	59470.33534	1800	32
WDJ060244.99–135103.57	DOZ V*	90.68749	–13.85096	INT/IDS(R400V)	59260.97692	1800	45
WDJ060244.99–135103.57	DOZ V*	90.68749	–13.85096	INT/IDS(R400V)	59261.91840	1800	44
WDJ061906.92–082807.15	DA	94.77885	–8.46865	VLT/X-Shooter	59314.02969	1800	60
WDJ061906.92–082807.15	DA	94.77889	–8.46865	INT/IDS(R400V)	58828.11719	1800	17
WDJ062145.32+065239.25	DA	95.43885	6.87757	VLT/X-Shooter	59314.00268	1800	54
WDJ062145.32+065239.25	DA	95.43883	6.87757	INT/IDS(R400V)	58828.0017	1800	19
WDJ064527.28+565916.90	DAe: V*	101.36365	56.98803	LBT/MODS	59528.28488	900	134
WDJ070204.29+051420.56	DOZ UHE V*	105.51790	5.23905	INT/IDS(R400V)	59261.02997	1800	67
WDJ070322.15–340331.94	DAO	105.84231	–34.05881	VLT/X-Shooter	60011.02962	1200	60
WDJ070647.52+613350.31	DA UHE V*	106.69800	61.56398	INT/IDS(R400V)	59261.10608	900	109
WDJ070647.52+613350.31	DA UHE V*	106.69800	61.56398	INT/IDS(R400V)	59261.08357	900	75
WDJ070647.52+613350.31	DA UHE V*	106.69800	61.56398	INT/IDS(R400V)	59261.09485	900	93
WDJ070647.52+613350.31	DA UHE V*	106.69800	61.56398	INT/IDS(R400V)	59262.94971	1100	102
WDJ073607.90+144451.07	DOZ	114.03290	14.74752	INT/IDS(R400V)	59261.12629	900	65
WDJ073957.35+091439.23	DA	114.98895	9.24423	INT/IDS(R400V)	58825.14766	1200	22
WDJ073957.35+091439.23	DA	114.98900	9.24423	INT/IDS(R400V)	59262.05103	1800	28
WDJ075134.71–015807.00	DO	117.89460	–1.96861	INT/IDS(R400V)	59261.99625	1800	40
WDJ075145.59+105931.36	DAe V*	117.93997	10.99204	LBT/MODS	59551.16308	900	94
WDJ080029.42–015039.82	DA	120.12258	–1.8444	INT/IDS(R400V)	58828.25166	1800	35
WDJ080326.15–034746.11	DAO	120.85896	–3.79614	VLT/X-Shooter	59281.16694	1800	60
WDJ080326.15–034746.11	DAO	120.85896	–3.79614	INT/IDS(R400V)	58828.22633	1800	32
WDJ080558.34+410931.84	DA V*	121.49307	41.15885	LBT/MODS	59528.36973	900	241
WDJ080950.28–364740.45	DAO	122.45944	–36.79449	VLT/X-Shooter	60014.14361	1200	50
WDJ085137.48+185119.67	DA	132.90615	18.85546	INT/IDS(R400V)	58825.2317	1800	36
WDJ093559.83+685201.55	DO UHE V*	143.99930	68.86710	LBT/MODS	59526.33673	900	118
WDJ120728.43+540129.16	DAO	181.86850	54.02477	INT/IDS(R400V)	59261.20041	1800	37
WDJ123952.73+720546.58	DA	189.96951	72.09627	INT/IDS(R400V)	59376.92141	900	36
WDJ125627.43+775301.37	DA UHE: V*	194.11430	77.88372	INT/IDS(R400V)	59261.24365	840	30
WDJ125627.43+775301.37	DA UHE: V*	194.11430	77.88372	INT/IDS(R400V)	59261.25424	840	48
WDJ132259.60–383813.13	sdO	200.74833	–38.63694	VLT/X-Shooter	59314.22414	1800	77
WDJ132307.79–480542.75	DAO	200.78246	–48.09521	VLT/X-Shooter	59987.32415	1200	86
WDJ134843.58+741545.75	DA	207.18159	74.26271	INT/IDS(R400V)	58837.25518	1800	43
WDJ134843.58+741545.75	DA	207.18154	74.26264	INT/IDS(R400V)	59376.89045	1800	39
WDJ135724.86+753723.60	DA	209.35335	75.62321	INT/IDS(R400V)	59375.99466	1800	35
WDJ135724.86+753723.60	DA	209.35359	75.62322	INT/IDS(R400V)	58836.23492	1800	49
WDJ142557.80–034139.92	DA	216.49080	–3.69442	INT/IDS(R400V)	59262.18566	1800	34
WDJ154843.31+472936.11	DOA	237.18036	47.49333	INT/IDS(R400V)	59377.90543	1200	30
WDJ160152.16+380455.24	DA	240.46730	38.08201	INT/IDS(R400V)	59262.15119	1800	32
WDJ165053.99+774844.88	DA	252.72426	77.81275	INT/IDS(R400V)	59375.94995	120	35
WDJ175145.75+382015.60	DA	267.94060	38.33767	INT/IDS(R400V)	59262.22048	1800	18
WDJ175629.64–072248.89	DA	269.12351	–7.38025	INT/IDS(R400V)	59377.03563	1800	43
WDJ181104.68+193658.10	DAO	272.76950	19.61614	INT/IDS(R400V)	59262.24628	1800	24

Table A.1. continued

Name	Type	Ra [deg]	Dec [deg]	Telescope/ Instrument	MJD-OBS	T_{exp} [s]	S/N
WDJ181104.68+193658.10	DAO	272.76950	19.61614	INT/IDS(R400V)	59262.26786	1800	32
WDJ182432.46+293115.88	DO	276.13524	29.52108	INT/IDS(R400V)	59376.0252	1800	48
WDJ182440.85−031959.52	DA	276.17028	−3.33329	INT/IDS(R400V)	59378.01071	900	36
WDJ182849.94+343649.94	DA	277.20809	34.61387	INT/IDS(R400V)	59377.92625	1800	36
WDJ182849.94+343649.94	DA	277.20809	34.61387	INT/IDS(R400V)	59377.92625	1800	31
WDJ183429.29+181101.71	DA	278.62208	18.18376	INT/IDS(R400V)	59376.11081	900	30
WDJ183429.29+181101.71	DA	278.62208	18.18376	INT/IDS(R400V)	59376.11081	900	27
WDJ184101.20+612032.16	DA	280.25499	61.34227	INT/IDS(R400V)	59376.97473	1800	37
WDJ190416.13−170153.08	DAO	286.06718	−17.03141	INT/IDS(R400V)	59379.07986	1500	27
WDJ190717.50+364000.37	DAO	286.82291	36.66677	INT/IDS(R400V)	59376.15473	900	33
WDJ191231.47−033131.86	DA	288.13102	−3.52566	INT/IDS(R400V)	59379.01501	900	43
WDJ191750.16−201409.55	DO	289.45901	−20.23599	INT/IDS(R400V)	59377.14625	1800	35
WDJ192705.33+112452.84	DA	291.77224	11.41463	INT/IDS(R400V)	59377.07346	900	66
WDJ194344.19+521732.66	DOZ	295.93412	52.29241	INT/IDS(R400V)	59377.0019	500	65
WDJ194511.31−445954.57	DAO	296.29703	−44.9985	VLT/X-Shooter	59427.16143	900	97
WDJ202547.32+355411.38	DA	306.44716	35.90316	INT/IDS(R400V)	59378.05155	900	34
WDJ210110.17−052751.14	DAO V*	315.29212	−5.46432	INT/IDS(R400V)	59377.22622	900	24
WDJ210110.17−052751.14	DAO V*	315.29212	−5.46432	INT/IDS(R400V)	59378.18389	900	28
WDJ210132.69+135622.59	DAO UHE V*	315.38619	13.93961	LBT/MODS	59528.34973	900	182
WDJ210824.97+275049.80	DAO	317.10403	27.84717	INT/IDS(R400V)	59378.15987	1500	30
WDJ211532.62−615849.50	DO UHE: V*	318.88590	−61.98035	VLT/X-Shooter	59469.26343	1800	65
WDJ211532.62−615849.50	DO UHE: V*	318.88590	−61.98035	SOAR/GHTS	59372.30922	800	40
WDJ212355.09+342017.32	DA	320.97954	34.33815	INT/IDS(R400V)	59378.06714	1200	30
WDJ214212.56+322052.17	DA	325.55249	32.34777	INT/IDS(R400V)	59379.2067	1500	32
WDJ214327.96+414318.99	DA	325.86627	41.72174	INT/IDS(R400V)	59379.05566	1500	26
WDJ215101.38−151839.71	DA	327.75574	−15.31103	INT/IDS(R400V)	59379.17214	1800	29
WDJ220247.69+275010.67	DA V*	330.69871	27.83630	LBT/MODS	59555.14628	900	74
WDJ220817.34+390711.18	DA	332.07226	39.11977	INT/IDS(R400V)	59378.11333	1500	22
WDJ222147.70+501150.75	DA V*	335.44874	50.19743	LBT/MODS	59526.07477	900	100
WDJ223522.88−494350.80	sdO	338.84547	−49.73088	VLT/X-Shooter	59409.3123	1800	63
WDJ224305.77+584336.70	DA	340.77417	58.72693	INT/IDS(R400V)	59377.17848	1500	43
WDJ225808.72+685751.45	DA	344.53632	68.96429	INT/IDS(R400V)	58834.90353	1800	40
WDJ231757.59+555026.25	DA	349.49002	55.84066	INT/IDS(R400V)	59378.13711	1500	27
GD1323	DAO	356.52117	−7.6516	VLT/X-Shooter	59765.37629	1800	78

Table A.2. Effective temperatures, surface gravities, radii, luminosities, gravity, HRD, and Kiel masses of the DA WDs.

Name (short)	T_{eff} [K]	$\log g$ [cm/s ²]	R [R _⊙ /100]	L [L _⊙]	M_{grav} [M _⊙]	M_{HRD} [M _⊙]	M_{Kiel} [M _⊙]
J0203-0639	60507±300	8.12±0.02	1.70±0.03	3.5 ^{+0.13} _{-0.12}	1.40 ^{+0.09} _{-0.08}	0.60±0.05	0.75±0.02
J0237+5834	70753±1820	8.04±0.1	1.55±0.04	5.4 ^{+0.7} _{-0.6}	0.96 ^{+0.26} _{-0.20}	0.67±0.06	0.73±0.05
J0314+3136	72664±1158	7.72±0.07	1.66±0.02	6.9±0.5	0.53 ^{+0.10} _{-0.08}	0.64±0.04	0.62±0.04
J0513-2259	70702±1426	7.8±0.08	1.39±0.02	4.3±0.4	0.44 ^{+0.10} _{-0.08}	0.72±0.04	0.64±0.04
J0538-1036	68255±1292	7.59±0.08	1.82±0.02	6.5 ^{+0.6} _{-0.5}	0.47 ^{+0.10} _{-0.08}	0.60±0.05	0.57±0.05
J0600-1014	63198±2099	7.51±0.11	1.50 ^{+0.03} _{-0.02}	3.2±0.5	0.26 ^{+0.08} _{-0.06}	0.67±0.05	0.54±0.04
J0619-0828	101921±1991	7.47±0.05	1.08±0.02	11.3 ^{+1.1} ₋₁	0.13 ^{+0.02} _{-0.02}	0.89±0.02	0.61±0.04
J0621+0652	108314±2186	7.63±0.05	1.75±0.05	38±4	0.48 ^{+0.07} _{-0.06}	0.70±0.04	0.65±0.05
J0645+5659	99762±3672	6.72±0.03	1.89 ^{+0.11} _{-0.10}	32 ⁺⁷ ₋₆	0.07 ^{+0.01} _{-0.01}	0.66±0.06	0.51±0.06
J0739+0914	81585±4449	7.17±0.11	1.89±0.07	14.2 ^{+3.6} ₋₃	0.19 ^{+0.06} _{-0.05}	0.62±0.06	0.52±0.05
J0800-0150	76169±5053	7.29±0.13	2.20 ^{+0.09} _{-0.08}	15 ⁺⁵ ₋₄	0.35 ^{+0.13} _{-0.10}	0.57±0.07	0.53±0.04
J0805+4109	50590±227	8.11±0.2	1.76±0.02	1.82±0.11	1.90±0.40	0.56±0.05	0.73±0.08
J0851+1851	70491±2125	7.87±0.12	1.57 ^{+0.05} _{-0.04}	5.5 ^{+0.8} _{-0.7}	0.67 ^{+0.23} _{-0.17}	0.66±0.06	0.66±0.06
J1239+7205	71049±2312	7.29±0.15	2.43 ^{+0.12} _{-0.11}	13.6 ^{+2.4} _{-2.1}	0.42 ^{+0.19} _{-0.13}	0.54±0.07	0.52±0.06
J1256+7753	68086±1723	7.71±0.1	1.88 ^{+0.03} _{-0.03}	6.8 ^{+0.8} _{-0.7}	0.66 ^{+0.18} _{-0.14}	0.59±0.06	0.61±0.05
J1348+7415	65092±2008	7.79±0.11	1.64 ^{+0.05} _{-0.04}	4.3 ^{+0.7} _{-0.6}	0.60 ^{+0.18} _{-0.14}	0.63±0.05	0.62±0.05
J1357+7537	51512±1065	7.86±0.09	1.32 ^{+0.02} _{-0.02}	1.11 ^{+0.1} _{-0.1}	0.46±0.10	0.70±0.04	0.62±0.05
J1425-0341	31795±268	7.39±0.07	2.14±0.04	0.422 ^{+0.02} _{-0.019}	0.41 ^{+0.07} _{-0.06}	0.47±0.03	0.46±0.03
J1601+3804	83236±7307	7.51±0.27	2.22 ^{+0.10} _{-0.09}	21 ⁺⁹ ₋₇	0.58 ^{+0.51} _{-0.27}	0.59±0.08	0.59±0.07
J1650+7748	29104±310	7.55±0.08	2.13 ^{+0.03} _{-0.03}	0.295 ^{+0.016} _{-0.015}	0.59 ^{+0.13} _{-0.11}	0.46±0.04	0.48±0.04
J1751+3820	69474±3314	6.71±0.16	2.88±0.08	17±4	0.15 ^{+0.07} _{-0.05}	0.51±0.06	0.43±0.06
J1756-0722	62941±1459	8.04±0.09	1.35±0.02	2.59 ^{+0.26} _{-0.24}	0.74 ^{+0.17} _{-0.14}	0.71±0.04	0.72±0.04
J1824-0319	68937±630	7.63±0.03	1.68±0.02	5.74 ^{+0.26} _{-0.25}	0.44±0.04	0.63±0.05	0.58±0.04
J1828+3436	39478±927	7.81±0.08	1.50±0.02	0.49±0.05	0.53 ^{+0.11} _{-0.10}	0.60±0.05	0.58±0.04
J1834+1811	57790±1685	7.38±0.11	2.13±0.04	4.6±0.6	0.40 ^{+0.12} _{-0.09}	0.52±0.05	0.51±0.06
J1841+6120	47322±897	8.02±0.1	1.36±0.02	0.84±0.07	0.71 ^{+0.18} _{-0.15}	0.67±0.04	0.68±0.05
J1912-0331	53271±1316	7.63±0.1	1.92 ^{+0.02} _{-0.02}	2.66 ^{+0.29} _{-0.27}	0.57 ^{+0.14} _{-0.12}	0.54±0.04	0.55±0.05
J1927+1124	77190±3559	7.54±0.11	1.69±0.05	9.2 ⁺² _{-1.7}	0.36 ^{+0.11} _{-0.09}	0.65±0.06	0.58±0.05
J2025+3554	35343±511	7.88±0.09	1.66 ^{+0.02} _{-0.02}	0.389 ^{+0.026} _{-0.024}	0.77 ^{+0.18} _{-0.15}	0.54±0.05	0.60±0.05
J2123+3420	57145±1858	7.79±0.13	1.75±0.04	2.9 ^{+0.5} _{-0.4}	0.69 ^{+0.25} _{-0.18}	0.59±0.05	0.61±0.05
J2142+3220	61309±2128	7.3±0.12	1.56 ^{+0.03} _{-0.03}	3.1±0.5	0.18 ^{+0.06} _{-0.05}	0.64±0.05	0.50±0.04
J2143+4143	83390±7284	7.24±0.25	1.84 ^{+0.08} _{-0.07}	15 ⁺⁷ ₋₅	0.22 ^{+0.17} _{-0.10}	0.63±0.09	0.54±0.06
J2151-1518	61511±2087	7.7±0.12	1.46±0.04	2.8 ^{+0.5} _{-0.4}	0.39 ^{+0.13} _{-0.10}	0.67±0.06	0.59±0.05
J2202+2750	58915±1135	8.25±0.17	1.78±0.07	3.5±0.4	2.10 ^{+1.10} _{-0.70}	0.58±0.05	0.82±0.06
J2208+3907	71826±2783	7.53±0.22	2.17±0.05	11.3 ⁺² _{-1.8}	0.58 ^{+0.39} _{-0.24}	0.56±0.05	0.57±0.06
J2221+5011	57480±552	7.95±0.04	1.52±0.05	2.27 ^{+0.17} _{-0.16}	0.75 ^{+0.09} _{-0.08}	0.64±0.04	0.67±0.03
J2243+5843	49918±850	7.76±0.07	1.59 ^{+0.02} _{-0.02}	1.41±0.11	0.52 ^{+0.10} _{-0.09}	0.60±0.05	0.58±0.05
J2258+6857	32424±290	8.08±0.06	1.17±0.01	0.137±0.006	0.60 ^{+0.10} _{-0.08}	0.73±0.04	0.69±0.03
J2317+5550	72758±3383	7.49±0.21	1.76±0.04	7.8 ^{+1.7} _{-1.4}	0.35 ^{+0.22} _{-0.14}	0.62±0.05	0.56±0.07

Table A.3. Effective temperatures, surface gravities, logarithmic He/H abundances ratios (by number), radii, luminosities, gravity, HRD, and Kiel masses of the DAO WDs, sdO, and O(H) stars.

Name (short)	T_{eff} [K]	$\log g$ [cm/s ²]	$\log(\text{He/H})$	R [R _⊙ /100]	L [L _⊙]	M_{grav} [M _⊙]	M_{HRD} [M _⊙]	M_{Kiel} [M _⊙]
GD 1323	112744±934	5.89±0.01	-1.00±0.01	8.80 ^{+0.01} _{-0.0100}	1120 ⁺³⁶⁰ ₋₂₅₀	0.22±0.07	0.52±0.05	0.55±0.02
J0703–3403	105839±734	6.77±0.02	-1.14±0.02	3.02±0.11	103 ⁺⁹ ₋₈	0.20±0.02	0.58±0.06	0.53±0.05
J0803–0347	86893±4625	6.86±0.12	-1.63±0.05	2.69 ^{+0.13} _{-0.12}	37 ⁺¹⁰ ₋₈	0.19 ^{+0.07} _{-0.05}	0.56±0.06	0.50±0.05
J0809–3647	103607±754	6.68±0.02	-1.18±0.02	3.22 ^{+0.12} _{-0.11}	108 ⁺⁹ ₋₈	0.18±0.02	0.57±0.06	0.52±0.06
J1207+5401	84918±11184	6.54±0.23	-0.99±0.08	4.50 ^{+0.50} _{-0.40}	90 ⁺⁷⁰ ₋₅₀	0.26 ^{+0.20} _{-0.12}	0.49±0.09	0.44±0.07
J1322–3838	80000±10000	6.00±0.50	-2.00±0.50	6.90 ^{+0.60} _{-0.50}	170 ⁺¹²⁰ ₋₈₀	0.17 ^{+0.38} _{-0.12}	0.42±0.07	0.42±0.07
J1323–4805	97563±808	6.87±0.02	-1.36±0.02	2.78 ^{+0.11} _{-0.10}	63 ⁺⁶ ₋₅	0.21±0.02	0.58±0.06	0.52±0.06
J1811+1936	83354±7075	6.71±0.17	-2.33±0.26	2.13 ^{+0.13} _{-0.12}	20 ⁺⁹ ₋₇	0.09 ^{+0.04} _{-0.03}	0.59±0.09	0.46±0.05
J1904–1701	81784±8778	6.76±0.26	-2.07±0.24	2.17 ^{+0.14} _{-0.12}	19 ⁺¹¹ ₋₈	0.10 ^{+0.09} _{-0.05}	0.59±0.08	0.46±0.06
J1907+3640	80924±10831	7.06±0.28	-1.18±0.11	2.46 ^{+0.19} _{-0.15}	23 ⁺¹⁷ ₋₁₁	0.25 ^{+0.24} _{-0.13}	0.56±0.11	0.51±0.06
J1945–4459	87559±1978	7.10±0.06	-1.81±0.07	2.37±0.05	29.8 ⁺³ _{-2.8}	0.26±0.04	0.58±0.04	0.53±0.03
J2101–0527	48904±265	8.14±0.06	-0.58±0.04	1.28±0.01	0.838 ^{+0.023} _{-0.022}	0.82 ^{+0.13} _{-0.11}	0.72±0.03	0.75±0.03
J2108+2750	80116±9176	7.00±0.26	-2.01±0.16	2.62 ^{+0.18} _{-0.15}	26 ⁺¹⁵ ₋₁₁	0.25 ^{+0.22} _{-0.12}	0.42±0.07	0.50±0.06
J2235–4943	75000±2161	6.06±0.04	-0.75±0.02	7.10 ^{+0.80} _{-0.70}	143 ⁺³⁹ ₋₂₉	0.21 ^{+0.06} _{-0.04}	0.41±0.04	0.40±0.03

Table A.4. Effective temperatures, surface gravities, logarithmic C/He abundance ratios (by number), radii, luminosities, gravity, HRD, and Kiel masses of the H-deficient WDs.

Name (short)	T_{eff} [K]	$\log g$ [cm/s ²]	$\log(\text{C/He})$	R [R _⊙ /100]	L [L _⊙]	M_{grav} [M _⊙]	M_{HRD} [M _⊙]	M_{Kiel} [M _⊙]
J0143+5841	116903± 631	7.87±0.04		1.08±0.04	19.6 ^{+1.4} _{-1.3}	0.31±0.04	0.88±0.02	0.69±0.03
J0334+1646	98383± 1085	7.87±0.03	-1.70 ± 0.30	1.64 ^{+0.10} _{-0.09}	22.8 ^{+3.1} _{-2.6}	0.73 ^{+0.11} _{-0.09}	0.65±0.08	0.67±0.05
J0436–0654	54451± 77	8.31±0.03		1.50±0.01	1.79±0.04	1.68 ^{+0.13} _{-0.12}	0.59±0.10	0.82±0.06
J0519–0443	72686± 3993	7.63±0.12		1.59±0.04	6.3 ^{+1.6} _{-1.4}	0.39 ^{+0.13} _{-0.10}	0.61±0.10	0.55±0.08
J0602–1351	100000±10000	7.50±0.50	-0.50 ± 0.20	1.99±0.11	36 ⁺¹⁸ ₋₁₃	0.46 ^{+0.47} _{-0.23}	0.58±0.12	0.56±0.13
J0736+1444	81319± 1599	7.92±0.03	-1.50 ± 0.30	1.48 ^{+0.02} _{-0.02}	8.7 ^{+0.8} _{-0.7}	0.67 ^{+0.06} _{-0.05}	0.66±0.07	0.66±0.05
J0751–0158	57013± 395	7.90±0.05		2.97 ^{+0.12} _{-0.11}	8.4±0.7	2.60 ^{+5.60} _{-1.80}	< 0.51	0.61±0.09
J1824+2931	54730± 66	8.27±0.03		1.34 ^{+0.02} _{-0.02}	1.44 ^{+0.05} _{-0.04}	1.21 ^{+0.10} _{-0.09}	0.66±0.02	0.80±0.02
J1917–2014	112649± 2839	8.00±0.10		3.05 ^{+0.18} _{-0.16}	135 ⁺²² ₋₁₉	3.40 ^{+1.00} _{-0.80}	0.53±0.04	0.74±0.05
J1943+5217	70601± 679	7.56±0.03	-2.20 ± 0.30	1.50±0.01	5.01±0.21	0.30 ^{+0.02} _{-0.02}	0.63±0.08	0.53±0.09
J2115–6158	70279± 914	7.56±0.03		1.56 ^{+0.03} _{-0.03}	5.3±0.4	0.32 ^{+0.03} _{-0.02}	0.61±0.08	0.52±0.10